

ARTICLE

<https://doi.org/10.1038/s41467-019-11475-4>

OPEN

Cellular responses to beating hydrogels to investigate mechanotransduction

Yashoda Chandorkar ¹, Arturo Castro Nava ¹, Sjören Schweizerhof ¹, Marcel Van Dongen¹, Tamás Haraszti ¹, Jens Köhler ¹, Hang Zhang ¹, Reinhard Windoffer ², Ahmed Mourran ¹, Martin Möller ¹ & Laura De Laporte ^{1,3}

Cells feel the forces exerted on them by the surrounding extracellular matrix (ECM) environment and respond to them. While many cell fate processes are dictated by these forces, which are highly synchronized in space and time, abnormal force transduction is implicated in the progression of many diseases (muscular dystrophy, cancer). However, material platforms that enable transient, cyclic forces in vitro to recreate an in vivo-like scenario remain a challenge. Here, we report a hydrogel system that rapidly beats (actuates) with spatio-temporal control using a near infra-red light trigger. Small, user-defined mechanical forces (~nN) are exerted on cells growing on the hydrogel surface at frequencies up to 10 Hz, revealing insights into the effect of actuation on cell migration and the kinetics of reversible nuclear translocation of the mechanosensor protein myocardin related transcription factor A, depending on the actuation amplitude, duration and frequency.

¹DWI - Leibniz-Institut für Interaktive Materialien e.V, Forckenbeckstr. 50, Aachen 52074, Germany. ²Institute of Molecular and Cellular Anatomy, Uniklinik, RWTH Aachen University, Aachen 52074, Germany. ³ITMC- Institute of Technical and Macromolecular Chemistry, RWTH Aachen University, Aachen 52074, Germany. Correspondence and requests for materials should be addressed to L.D.L. (email: delaporte@dwi.rwth-aachen.de)

The extracellular matrix (ECM) is dynamic and undergoes constant remodelling, partly due to forces exerted by the cells. Therefore, the ECM provides changing mechanical cues to the periphery of the cells, which are again conveyed by the cells to their internal machinery affecting cell behaviour. This communication process is called mechanotransduction and takes place in a continuous feedback cycle. A disruption in force transmission is associated with many pathologies and diseases, ranging from arteriosclerosis, muscular dystrophy and cancer^{1,2}. Importantly, many soft tissues, such as the heart, blood vessels³, lungs⁴ and cartilage⁵ often experience cyclic, rather than constant strains. Deciphering this language of forces is, however, hindered due to the lack of *in vitro* systems that can generate and regulate forces on cells that mimic natural stresses. For example, low throughput cell-selective manipulation techniques that target individual cells, including optical tweezers, atomic force microscopy, and magnetic bead cytometry^{6,7}, resemble acute, invasive stresses (cell poking), which may damage the cells by affecting their cortical shell^{8,9}. On the other hand, more realistic stresses can be applied by a growth substrate via stretching devices (e.g. Flexcell, USA). Here, cells are grown on flat or patterned stiff polydimethylsiloxane (PDMS) elastomer sheets (elastic modulus (E) ~ 2 MPa) and exposed to oscillating strains consisting of amplitudes ranging from 0 to 23% and frequencies as high as 5 Hz (higher frequencies limit achievable maximal strains)^{10–12}. A majority of systems have a large response time (\sim s) and are restricted to generate unidirectional or bi-directional forces without spatial control of the region, in which cells are affected.

To manipulate cells with precisely controlled mechanical forces in space and time, one other approach grows cells on cell-adhesive stiff elastomeric micropillars (Norland Optical Adhesive (NOA), $E \sim 1$ GPa) that are embedded in a thermoresponsive, non-cell-adhesive poly N-isopropyl acrylamide (PNIPAM) hydrogel containing gold nanorods (AuNRs) as photothermal transducers. Light triggered local change of the hydrogel results in bending of the elastomeric micropillars¹³, which substitutes the electrical motors used in traditional cell stretching devices. In contrast to natural substrates, where cells are free to grow and attach, here cells are restricted to attach to the micropillars, which limits their spreading and migration behaviour. This technique uses relative low frequencies up to 0.1 Hz and does not stimulate cells for long periods of time, hence no link with mechanical cell signalling pathways was revealed. To better mimic the ECM and grow cells on 2D¹⁴ or in 3D^{15–18}, soft hydrogels ($E \sim 0.1$ –100 kPa) are often used. While most traditional elastic, flat and static hydrogels do not represent the dynamic nature of native ECM, some engineered hydrogel materials enable spatio-temporal changes in a unidirectional manner using external triggers¹⁸, such as light-induced softening^{19,20} or stiffening²¹ that cannot be reversed. Only a few hydrogel systems offer dynamic, reversible changes in mechanical properties without spatial control^{22–24} or undergo slow transitions (in the order of days²⁵, hours²⁴ or minutes^{26–28}), while others are not compatible with cells²⁹. Currently, to the best of our knowledge, no soft hydrogel systems are available that facilitate both cell adherence and reversible, cyclic mechanical property changes up to 10 Hz with precise spatial control.

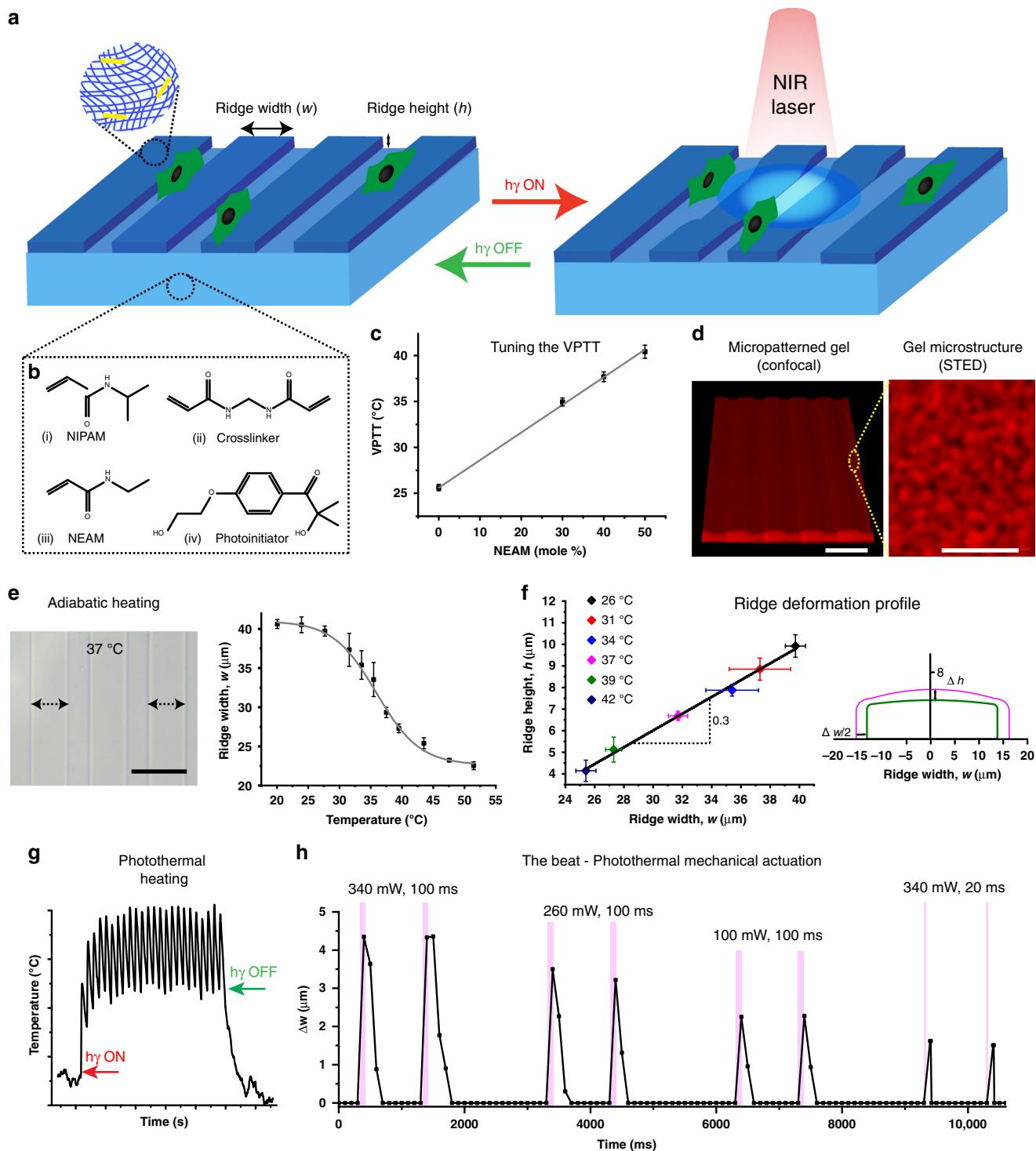
Here, we demonstrate a light-responsive hydrogel platform, which supports unrestricted cell growth and reversibly applies precise and user-defined mechanical forces on selected cells under physiological conditions. This approach comprises a soft and patterned thin-film ECM-mimetic hydrogel prepared with a ratio of 60/40 mole % N-isopropyl acrylamide (NIPAM) and N-ethyl acrylamide (NEAM) to achieve a volume phase transition temperature (VPTT) around 37 °C, AuNRs for photothermal heating, and a fibronectin/collagen I surface coating for cell attachment

(Fig. 1a). Cells grow at ~ 36 °C and the gel exhibits local mechanical actuation (beats) with a specific amplitude for an indefinite length of time at variable frequencies up to 10 Hz using a near infra-red (NIR) laser as light trigger. Precise, transient forces generated can be controlled at a user-defined sub-cellular or sub-population scale that is not pre-determined during gel fabrication. The direction of applied forces can be changed by the pre-defined topography of the hydrogel. As proof of principle, a subset of L929 fibroblast cells is actuated, resulting in changes in cell migration and nuclear translocation of the mechanosensor protein myocardin related transcription factor A (MRTFA), depending on the duration, amplitude and frequency of actuation. The Yes-associated protein (YAP) remains in the nucleus before, during and after actuation.

Results

Defining the photothermal actuation beat. Thin hydrogel films with micropatterns that are confined to a glass coverslip are prepared with a NIPAM/NEAM molar ratio of 60/40% to achieve a VPTT ~ 37 °C in the presence of cell culture media (Fig. 1b, c, Supplementary Fig. 1, 2, Supplementary Note 1). Unless otherwise mentioned, these gels are used for all experiments and referred to as gels or hydrogels. The gels are formed on a silicon wafer with continuous arrays of elevated ridges of 25 μ m width and 2.7 μ m height, separated by 25 μ m valleys, while their internal structure is porous (Fig. 1d).

Adiabatic heating (in thermal equilibrium) of the entire gel (Fig. 1e, f) results in deformation of the microtopography. The ridge width (w) shrinks from ~ 40 to 24 μ m over a temperature range of 26–42 °C, while the ridge height (h) shrinks from ~ 10 to 4 μ m (Fig. 1f). Ridge deformation is predominant in the lateral direction (Δw) as compared to the axial direction (Δh) ($(\Delta h)/(\Delta w) \sim 0.3$), in contrast to flat confined gels³⁰ (Fig. 1f, Supplementary Note 2). A comparison of the lateral swelling ratio for the ridges (~ 1.8) with that for free-standing hydrogel discs (~ 1.6), (Supplementary Fig. 3, Supplementary Table 1) suggests that the confinement of the patterned hydrogel film, tethered to a glass coverslip does not significantly affect the swelling and shrinking ability of the ridges. In contrast to reported literature on confined gels³⁰, creases are avoided by keeping a ridge filling fraction of 0.5 (Supplementary Fig. 4, Supplementary Note 2). To render the gels photoresponsive, PEG-stabilised AuNRs are added to the precursor solution before gelation at a concentration of ~ 3.6 AuNRs/ μ m³, corresponding to a volume fraction of 0.004% AuNRs (Supplementary Fig. 5). Due to the photothermal effect of the AuNRs, the temperature of the irradiated gel area increases, resulting in a local gel collapse. In the case of stroboscopic illumination using a NIR laser, rapid gel actuation is achieved in the milli-second range. While adiabatic heating reflects the maximum extent of mechanical deformation and does not show spatial selectivity, local photothermal heating results in local temperature shifts that cause volume transitions (non-equilibrium), corresponding to the stroboscopic input. (Fig. 1g, h). The laser pulses (frequency and duty cycle) and power are varied to alter the amplitude and frequency of actuation. Spatially controlled actuation of the gel is achieved in a user-defined region of the gel (Movie 1, 340 mW, 1 Hz, ON time 100 ms, higher magnification in Movie 2). The non-irradiated region of the gel does not actuate and thus functions as a control region. The ridge lines are considered as reference points to measure the total change in ridge width, with the maximum change during one laser pulse defined as the amplitude, which changes from ~ 4.3 to 1.6 μ m for different laser settings (100 ms and 20 ms laser ON time, Movie 2 and 3, respectively, Fig. 1h, Supplementary Table 2). During the recovery time when the laser



is off, the gel cools down and re-swells before the light is back on (Supplementary Note 3). As the mesh size of similarly crosslinked hydrogels is reported to be ~5 nm, it can safely be assumed that the AuNRs are trapped inside the gel³¹. Inductively coupled plasma-optical emission spectroscopy (ICP-OES) confirms that the AuNRs do not leach out from the crosslinked hydrogel after swelling for 3 days (Supplementary Fig. 5e). The presence of these low amounts of AuNRs inside the gel does not affect the volume phase transition behaviour (Supplementary Fig. 6).

To decouple the effect of mechanical actuation from photothermal heating of the gel, two controls are performed; one to investigate the effect of light exposure and one to test the impact

of photothermal heating, both without mechanical actuation at ~36–37 °C. For the first control, 60/40 NIPAM/NEAM gels without AuNRs are used (light, no heat, no deformation), while the second control comprises gels made with 100% NEAM (LCST ~82 °C) and AuNRs (3.6 AuNRs/μm³) (light + heat, no deformation). The local temperature changes that occur when the gels are irradiated with a NIR laser at 340 mW, 1 Hz and 100 ms laser ON time are measured with an IR camera (Fig. 2a–c, Supplementary Fig. 7a). The gels with AuNRs show photothermal heating, while no such effect is observed for the control gel without AuNRs (Fig. 2d–f). The temperature corresponding to the thermograms is quantified over time (Fig. 2g–i), demonstrating a mean total

Fig. 1 Thermoresponsive hydrogels that respond to a light trigger for rapid actuation. **a** Schematic showing the concept of actuating gels. Soft and patterned thin-film hydrogels are prepared from a thermoresponsive polymer. The gel contains AuNRs and is covalently bound to a glass coverslip. When a NIR laser shines on the gel, the AuNRs convert light to heat and the temperature of the gel locally increases to collapse the gel; therefore, a pulsing laser results in actuating (beating) gels. **b** The gel films are prepared with 57 wt% NIPAM and NEAM monomers at different ratios, 1 mole % crosslinker (N, N'-methylenebisacrylamide), and 1 mole % photo-initiator (2-hydroxy-4-(2-hydroxyethoxy)-2-methylpropiophenone). **c** The VPTT of the gels is tuned to 37 °C with a NIPAM/NEAM ratio of 60/40 mole %, $n = 3$. **d** 3D confocal stack of a hydrogel film with 25 μm ridges and 25 μm valleys, scale bar = 50 μm . STED microscopy of gels at 37 °C, showing the microstructure of the gel, scale bar = 1 μm . **e** A representative brightfield image of a 60/40 % NIPAM/NEAM patterned gel at 37 °C. The VPTT for gels is calculated from changes in the ridge width at different temperatures in thermal equilibrium and adiabatic conditions, scale bar = 50 μm , $n = 3$. **f** The actuation beat is represented by the gel deformation with respect to the ridge width and height at different temperatures under adiabatic conditions, showing $\Delta h/\Delta w \sim 0.3$, $n = 3$. The illustration (drawn to scale) depicts the ridge shape at 37 and 39 °C. **g** Schematic of photothermal heating resulting in temperature changes of the gel that are synchronised with the laser pulses. **h** Due to local temperature changes, small changes in the ridge width (mechanical deformation, the beat) are also synchronised with the laser. The amplitude is defined as the maximum change in ridge width and is controlled by reducing laser power from 340 to 260 to 100 mW for a 100 ms pulse at 1 Hz or by changing the pulse duration to 20 ms at 340 mW at 1 Hz. Error bars represent standard deviation

increase (averaged over the irradiated area and compared to the averaged ground state before light exposure) ΔT_{mean} of ~ 0.9 °C. The photothermal effect leads to a new thermal equilibrium state during actuation ($\delta T_{\text{mean}} \sim 0.6$ °C higher than the ground state before light exposure) around which the gel temperature oscillates ($dT_{\text{mean}} \sim \pm 0.3$ °C) during pulsing, synchronised with the laser pulse (Fig. 2g–j, Movie 4, 5). The ridge deformation amplitudes remain constant for 22 h of actuation, which suggests that the temperature does not increase when pulsed for a prolonged time and that it is possible to stay close to the physiological temperature by minimising dT_{mean} during actuation. The maximum temperature increase, ΔT_{max} , (determined from the maximum temperature measured in the irradiated portion of the gel compared to the temperature before light exposure) is ~ 3.0 °C, while the maximum temperature oscillations around the new equilibrium (dT_{max}) are $\sim \pm 1.5$ °C, keeping the maximum temperature (due to positive fluctuations) below 39.0 °C and thus below the temperature of heat shock for cells³² (Supplementary Fig. 7b,c, Supplementary Note 4). This maximum temperature is not experienced throughout the actuated region but spatially confined and in tandem with the laser pulses. The temperature returns to the new equilibrium in ~ 700 ms after a 100 ms pulse is fired (Fig. 2l, Movie 5), which is in agreement with the estimated temperature based on a thermal calibration curve (Fig. 1e, Supplementary Note 4). The experimental temperature observations are supported by simulation data using finite element analysis (Supplementary Fig. 8, Supplementary Note 5, Supplementary Table 3), where a total mean temperature increase (dT) of ~ 1.8 °C is expected due to NIR irradiation. To test the effect of temperature on cell proliferation, cells are grown on tissue culture polystyrene (TCPS) for 24 h, revealing no significant difference between 30 and 40 °C, while cell proliferation at 25 and 45 °C is reduced (Supplementary Fig. 9a). Exposure to 44–45 °C for 2 h is known to cause thermal shock leading to over expression of the heat shock protein (Hsp 70)³³. Stress granules made of non-translating mRNA and P bodies that contain proteins, which decay mRNA, are generated in response to oxidative, osmotic, heat or UV irradiation stresses or viruses³⁴. Therefore, the levels of Hsp 70, along with stress granules and P bodies, are quantified and compared for actuated vs. non-actuated cells by immunofluorescence, demonstrating no significant difference between both conditions (Supplementary Fig. 9), suggesting that cells are not unduly mechanically or thermally stressed due to actuation.

Cell migration and mechanotransduction affected by actuation. Cells are seeded on fibronectin coated 60/40 NIPAM/NEAM hydrogel films and allowed to adhere for ≥ 12 h, after which the gels are actuated (Supplementary Fig. 10). Fibronectin

is covalently linked to the gel using optimised conditions (Supplementary Fig. 11, Supplementary Note 6). An exposure to NIR light (340 mW, 1 Hz, 100 ms ON time) during the time course of 22 h does not affect cell viability as shown using a live-dead assay for 60/40 NIPAM/NEAM gels in the actuated and non-actuated area (Supplementary Fig. 11e). A representative brightfield 12 h time-lapse video of cells on the surface of actuating hydrogels (340 mW power, 1 Hz, 100 ms ON time) is shown in Movie 6. Cell motility parameters are measured for individual cells on actuating gels and compared against cells on control, mechanically invariant gels of 100% NEAM, which do not actuate.

On both the actuated and control gels, cells move erratically along the ridges (Fig. 3a–c, Supplementary Fig. 12, Supplementary Note 7) with a reduced migration rate (~ 5 and ~ 7.5 $\mu\text{m}/\text{h}$ for the actuated and the control gel, respectively) and increased persistence (~ 0.6 in the case of actuated cells while ~ 0.4 for the control), while the end-to-end distance of the trajectories (the net displacement of cells from the initial position to the final position) is not affected by actuation (mean ~ 50 μm) in ~ 12 h, (Supplementary Fig. 12). Persistence is a good indicator of the effect of structural guidance provided by the gel topography; actuating gel topography further enhances cell movement along the topography. The projected contour length, (the distance travelled by cells in the direction of the ridges) remains higher for non-actuated gels (~ 75 μm as compared to ~ 50 μm with actuation, $\sim 33\%$ decrease) due to the overall higher migration rate. To mechanistically explain slower cell migration on actuating surfaces, the focal adhesions (FA) on cells actuated for 12 h (340 mW, 1 Hz, 100 ms laser ON time) are stained against vinculin and paxillin and compared to non-actuated cells (Fig. 3d–j). Actuation leads to an increase in the number of focal adhesions per cell (from $\sim 15/\text{cell}$ to $\sim 24/\text{cell}$, $\sim 60\%$ increase upon actuation), while the size of focal adhesions and the net area ($\text{Area}_{\text{FA}}/\text{Area}_{\text{cell}}$) occupied by focal adhesions per cell remain the same in both the cases. This suggests that actuation leads to greater cellular adhesion to the substrate through more focal adhesions resulting in a larger cellular spread area.

During cell adhesion and migration, actin filaments in the cytoskeleton undergo dynamic changes. Globular actin (G-actin) is polymerised to form actin filaments (F-actin) and generates the forces necessary to establish focal adhesions and protrude lamellipodial or filopodial extensions³⁵. The myocardin related transcription factor A (MRTFA) is known to be associated with cytoskeletal dynamics and is a direct measure of the G-actin concentration in the cell, as it releases G-actin and shuttles to the nucleus^{35–37}. Another protein that has occupied a centre-stage in understanding mechanobiology is the Yes-associated protein (YAP), which can respond to a variety of mechanical cues, such as

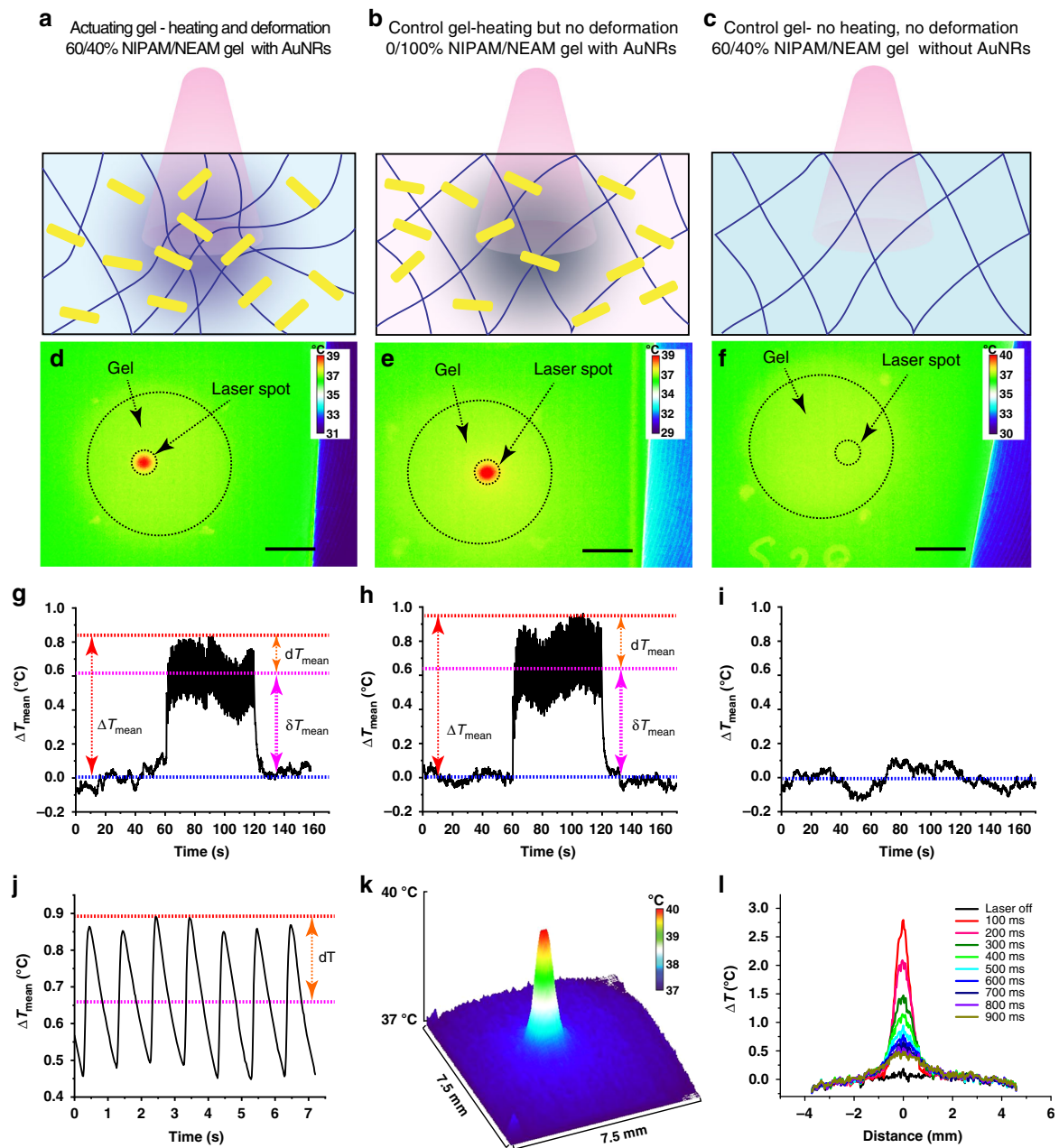
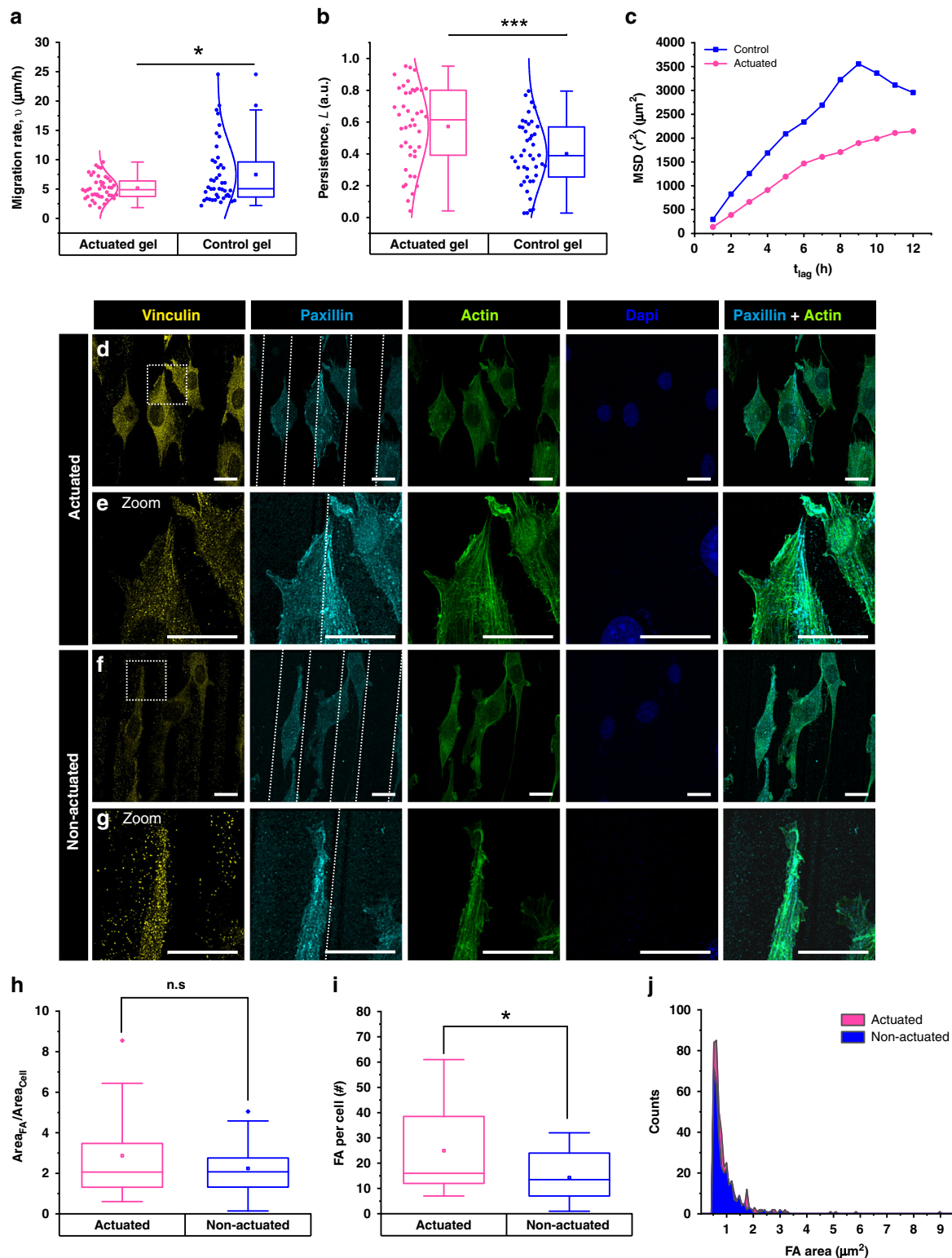


Fig. 2 Temperature modulation during actuation does not exceed hyperthermia temperature. A schematic of **a** 60/40 NIPAM/NEAM gels with AuNRs, which actuate and show temperature changes when irradiated with NIR light, **b** 0/100 NIPAM/NEAM gels with AuNRs, which show a temperature gradient but do not actuate when irradiated with NIR laser, **c** 60/40 NIPAM/NEAM gels without AuNRs, which do not actuate or generate a temperature gradient when irradiated with NIR laser. The temperature gradient is depicted with color shading and the deswelling is shown by changes in the mesh size (not to scale). **d-f** Representative thermal images obtained during photothermal heating of the gels for **a-c**, respectively, scale bar = 3 mm. The laser is turned on at -60 sec (340 mW, 1 Hz, 100 ms laser ON time) and turned off at -120 sec. **g-i** Temperature profiles for the pulsed laser, calculated from images as depicted in **d-f**, respectively. **j** The mean temperature of the irradiated portion of the gel oscillates with the laser frequency. **k** A surface plot of the gel temperature, showing the spatial control of actuation. **l** The spatial temperature profile changes with the laser pulse, which is turned on at $t = 0$ ms. (340 mW, 1 Hz, 100 ms ON time)

substrate rigidity and topologies affecting cell geometry³⁸. The intracellular localisation of YAP is considered to depict the substrate stiffness, as it is mostly localised in the nucleus when cells are grown on stiff elastic substrates (>30 kPa) and in the cytoplasm when cells are grown on soft elastic substrates (≤ 5 kPa)³⁹.

After actuation, cells are immunostained against MRTFA and YAP. In the case of MRTFA, a distinct translocation from the cytoplasm to the nucleus is observed, depending on the laser

settings and duration of exposure. The cells growing outside the exposed region on the same gel function as control cells and do not show MRTFA shuttling (quantified to give Nuclear MRTFA %, Supplementary Fig. 13). On the control gels, 0/100 NIPAM/NEAM with AuNRs (heating, no mechanical deformation) and 60/40 NIPAM/NEAM gels without AuNRs (no heating, no mechanical deformation), MRTFA also remains in the cytoplasm (Supplementary Fig. 14). Additionally, to show that MRTFA is not affected by temperature, cells are cultivated at 36 °C and 39 °C



under static conditions on top of the hydrogel film (Supplementary Fig. 15). In both cases, MRTFA is present in the cytoplasm. These control conditions assist in decoupling the effect of mechanical actuation from other factors, such as gel topography, light, temperature and photothermal heating, with only minimal changes in stiffness upon actuation.

When the duration of actuation is varied from 4, 8, 12 to 22 h, the nuclear signal of MRTFA gradually increases when the ridges shrink and swell with an amplitude of $\sim 4.3 \mu\text{m}$ ($\sim 14\%$

deformation, 340 mW, 1 Hz, 100 ms ON time). Fluorescence intensity quantification of MRTFA in the nucleus and cytoplasm (Fig. 4, Supplementary Fig. 16) shows that after 4 h of actuation, nuclear MRTFA accumulation is not yet visible but nuclear translocation starts around 8 h. The MRTFA levels in the nucleus further increase after 12 and 22 h. For non-actuated cells, the distribution of MRTFA is uniform across the cell population, while a broader distribution is visible upon actuation. Although accumulation in the nucleus is higher at 22 h (75%), the 12 h time

Fig. 3 Linking actuation effects on cell migration to focal adhesions. **a, b** Box plots showing cell motility parameters on 60/40 NIPAM/NEAM gels as a result of gel actuation, in comparison to non-actuating 0/100 NIPAM/NEAM control gels, **a** the migration rate **b** the persistence. The end-to-end distance, the contour length and the projected contour length can be found in Supplementary Fig. 12. **c** The Mean Squared Displacement as a function of lag times. ($n = 2$, $N \geq 43$ cells). **d–g** Effect of actuation on the formation of focal adhesions is investigated using vinculin and paxillin immunofluorescence. **d, e** Cells are actuated for 12 h (340 mW, 1 Hz, 100 ms laser ON time), **e** shows a magnification of the dotted square in **d**. The edges of the ridge are marked by white dotted lines, showing an increase in focal adhesions along the ridge edges. **f, g** Control cells that are not irradiated with the laser and hence, not subject to actuation, with **g** showing a magnified image of the dotted square marked in **f**. **h** The total area occupied by all focal adhesions per cell. **i** The total number of focal adhesions per cell for the actuated and the non-actuated conditions are represented by box plots, which increase due to actuation. **j** Histogram of the area of focal adhesions for the actuated vs. the non-actuated cells ($n = 3$, $N \geq 17$ cells). In the box plots, the interquartile range (IQR) between the first and the third quartiles is indicated by the box, while whiskers denote 1.5 IQR. The hollow square, the horizontal line, and the filled dots represent the average, the median, and the outliers, respectively. On the left of the box plot, all data points are shown, the normal distribution curve serves to guide the eye. *, **, *** are determined using one way ANOVA or Welch test, depending on the homogeneity of variances, and represent statistical significance at $p < 0.05$, 0.01 and 0.001, respectively. **d–g** Scale bar = 20 μm

point is further used throughout this study as the doubling time of the L929 cell line is ~ 24 h.

To investigate the effect of amplitude on MRTFA translocation, the laser output power is decreased from 340 to 260 to 100 mW, while maintaining the frequency of actuation at 1 Hz (100 ms ON time) for a duration of 12 h. A laser power of 100 or 260 mW, corresponding to an actuation amplitude of 2.2 or 3.2 μm , respectively, causes less MRTFA shuttling to the nucleus with nuclear MRTFA levels of $\sim 30\%$ in both cases compared to $\sim 50\%$ in the case of 340 mW, which is still significantly higher than for non-actuating controls ($\sim 20\%$) (Fig. 4b, f, Supplementary Fig. 17). Another way to control the amplitude of oscillation is by varying the duration of the pulse (ON time), for example a reduction from 100 to 20 ms (340 mW, 1 Hz) leads to an amplitude of ~ 2.0 μm instead of ~ 4.3 μm and less nuclear accumulation ($\sim 40\%$ instead of $\sim 50\%$) (Fig. 4b, g, Supplementary Fig. 18). Interestingly, a similar reduction in amplitude by lowering the laser power to 100 mW (1 Hz, 100 ms ON time) has less effect on MRTFA translocation.

For an ON time of 100 ms, and frequencies of 1, 0.5 and 0.1 Hz, respectively (laser output 340 mW, 12 h) (Fig. 4c, h, Supplementary Fig. 19), a frequency of 1 Hz results in the highest nuclear accumulation of $\sim 50\%$, compared to $\sim 40\%$ for 0.5 or 0.1 Hz. The ON time is reduced to 20 ms to achieve frequencies of 1, 5 and 10 Hz (Fig. 4c, i) where 1 Hz leads again to the highest nuclear MRTFA levels ($\sim 45\%$, a bit less than for 100 ms ON time). Therefore, in these experiments, the most prominent effect is always seen at a frequency of 1 Hz.

To check the reversibility of this translocation, irradiation (340 mW power, 1 Hz, 100 ms ON time) is stopped after 12 h and the gel is allowed to relax for different durations (Fig. 4d, j, Supplementary Fig. 20). After cessation of actuation for 2.5, 5, 10 and 14 h, the nuclear % of MRTFA slowly drops from 50 to 45 to 40 to 35%, respectively and approaches the initial value of 20%. Therefore, it appears that the return kinetics for MRTFA from the nucleus to the cytoplasm is slower than nuclear translocation. To rule out the possibility that the fibrillar nature of the fibronectin coating affects the cell response to actuation⁴⁰, cells are actuated on collagen I coated gels, revealing a similar nuclear translocation of MRTFA (Fig. 5a, b, Supplementary Fig. 21). Interestingly, actuated fibroblasts secrete more fibronectin (~ 33 counts/px), which is also aligned, as compared to the random nature and lower concentration of fibronectin secreted by non-actuated cells (25 counts/px) (Fig. 5c–e, Supplementary Fig. 22). These results are in agreement with the MRTFA nuclear shuttling, which is known to activate focal adhesion stabilising genes and reduce cell migration⁴¹. They suggest that the increase in fibronectin production in the case of actuating cells may contribute to long-term environmental changes that affect the cells further, for example the increase in MRTFA accumulation in the nucleus at

later time points (~ 8 h) and the fact that, after turning off the light, the MRTFA only partially shuttles back to the cytoplasm.

On the other hand, when immunostaining for YAP, it is clear that YAP is located in the nucleus for both the actuated and non-actuated gel (340 mW power, 1 Hz, 100 ms ON time, 12 h, Supplementary Fig. 23). This may be explained by the stiffness of the hydrogel film at 37 °C near the VPTT ($E \sim 30$ kPa, AFM, Supplementary Fig. 24, Supplementary Note 1), promoting nuclear accumulation of YAP, which is also similar to the rigidity threshold for unfolding of talin^{39,42}. This argument is supported by our control experiments, where YAP is located in the nucleus when cells are grown on stiff TCPS ($E = 2$ GPa)⁴³ and in the cytoplasm when cells are grown on ultra-soft 1 wt % poly (ethylene glycol) (PEG) gels ($G' = 20$ Pa)⁴⁴, while under these circumstances, MRTFA is always found in the cytoplasm (Supplementary Fig. 25)

Discussion

Soft tissues are often subjected to shear stress and cyclic mechanical strains¹². While these forces are essential in maintaining a healthy physiology of different organs and tissues, a deviation leading to abnormal mechanical forces can result in disease. Therefore, in vitro platforms are required to replicate mechanical forces on cells and tissues to understand the key mechanosensor molecules involved in mechanotransduction and signalling pathways. This work demonstrates a smart hydrogel platform that can actuate to mechanically stimulate cells in a cyclic, user-defined manner. Since the modulus of the gels is sufficiently low, frequencies as high as 10 Hz are achieved, which is up to 2 orders of magnitude higher than other stretching systems reported in literature (0.1 Hz)¹³. The local actuation of the gel depends on the heat generation by the AuNRs, which is governed by the optical properties and concentration of the AuNRs and the intensity of the laser spot on the sample (laser fluence)⁴⁵. The AuNR concentration of 3.6 AuNRs/ μm^3 does not affect the VPTT but is sufficiently high to enable the use of relatively low laser flux and laser on time ($0.7\text{--}3.6 \times 10^3$ W/cm³ for 20–100 ms), which is 2 orders of magnitude less than the 3.6×10^5 W/cm³ for up to 5 min reported in literature¹³. Based on measurements, $\sim 2.5\text{--}7\%$ relative displacements are achieved with a δT_{mean} of $\sim 0.1\text{--}0.6$ °C, respectively (Supplementary Fig. 26, Supplementary Table 2, Supplementary Method 8).

Due to actuation of the hydrogel film, the cell migration rate is reduced, while the persistence of cells increases. In addition, MRTFA shuttles to the nucleus after 8 h depending on the frequency (maximum effect at 1 Hz), amplitude, and duration of actuation. It is likely that 1 Hz is a threshold value for the frequency, at which saturation of the cellular response occurs. Below this frequency, there may be limiting factors, such as insufficient reorganisation of the actin cytoskeleton and focal adhesions at

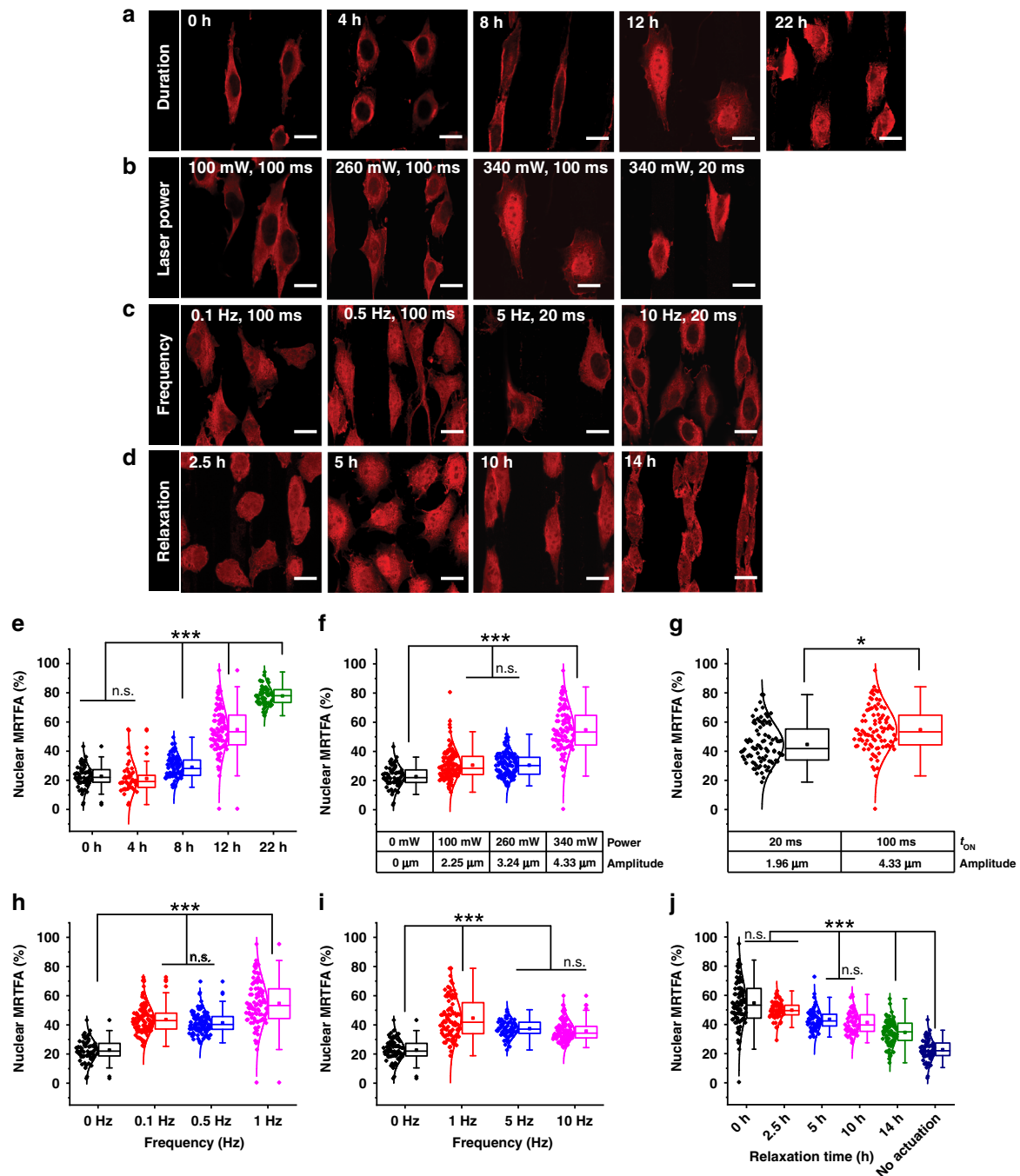


Fig. 4 Immunofluorescence images showing the distribution of MRTFA in the cells. **a** Cells are actuated for 0, 4, 8, 12 and 22 h (340 mW, 1 Hz, 100 ms laser ON time), **b** The actuation amplitude is varied by using a laser power of 100 mW, 260 mW or 340 mW (1 Hz, 100 ms ON time, 12 h actuation), or by reducing the laser pulse to 20 ms at 340 mW laser power and 1 Hz frequency. **c** Cells are actuated at 0.1 Hz and 0.5 Hz at 340 mW (100 ms ON time, 12 h actuation), while higher frequencies of 5 Hz and 10 Hz are obtained using a shorter ON time of 20 ms, keeping the laser power constant (340 mW). **d** After actuating for 12 h (340 mW, 1 Hz, 100 ms laser ON time), actuation is ceased and cells are allowed to relax for 2.5, 5, 10 and 14 h. **e–j** The nuclear MRTFA % is measured to assess the effect of **e** duration of actuation, **f** actuation amplitude by changing laser output, **g** actuation amplitude by changing the ON time of the laser pulse, **h** frequency when ON time = 100 ms, **i** frequency when ON time = 20 ms and **j** relaxation. Scale bar = 20 μm . The box plots show the nuclear MRTFA % for each cell ($n \geq 3$, $N \geq 60$ cells, except **e**, where $N \geq 48$ cells). In the box plots, the interquartile range (IQR) between the first and the third quartiles is indicated by the box, while whiskers denote 1.5 IQR. The hollow square, the horizontal line, and the filled dots represent the average, the median, and the outliers, respectively. On the left of the box plot, all data points are shown, the normal distribution curve serves to guide the eye. *, **, *** are determined using one way ANOVA or Welch test, depending on the homogeneity of variances, and represent statistical significance at $p < 0.05$, 0.01 and 0.001, respectively

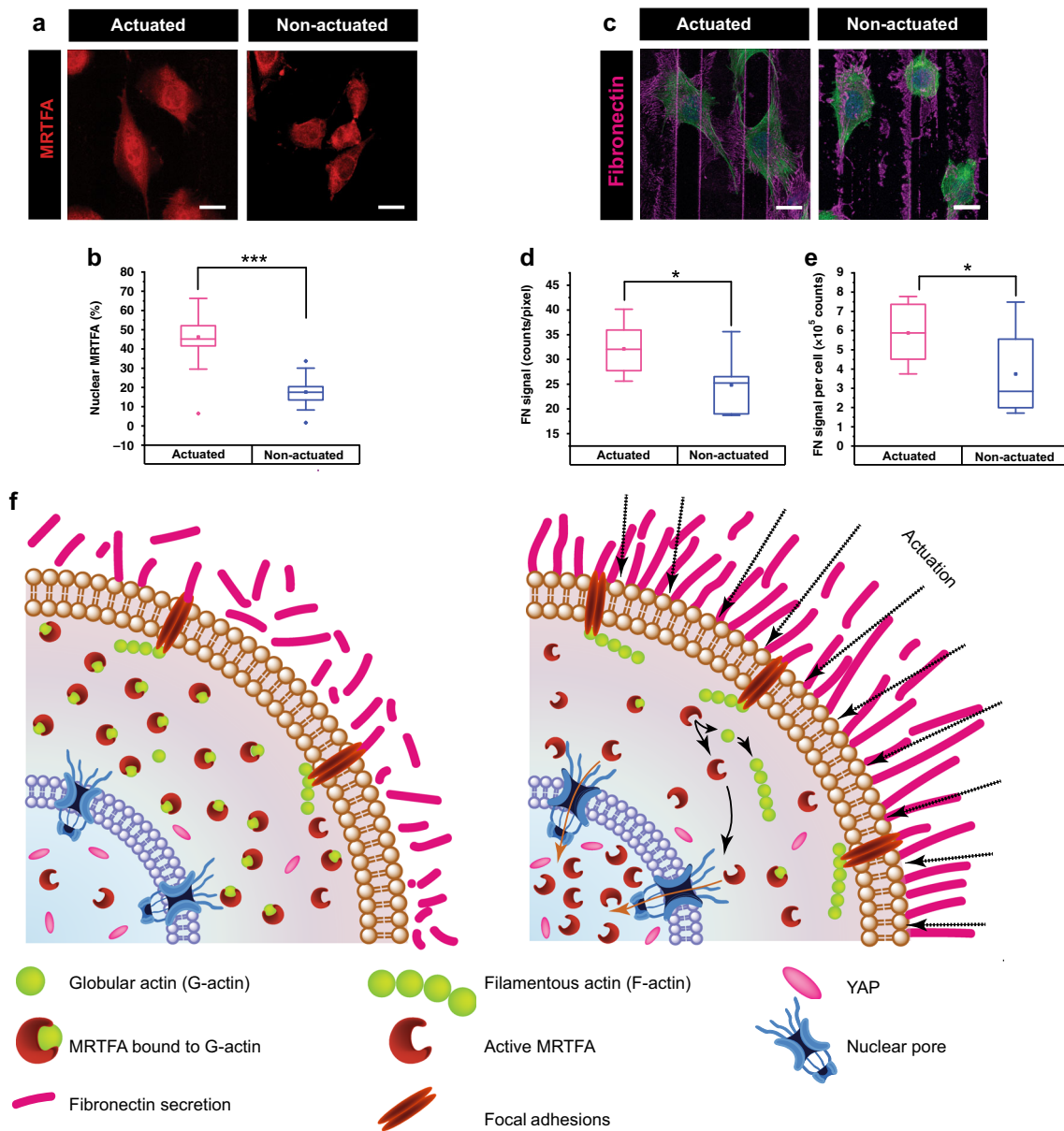


Fig. 5 The effect of actuation on mechanosensitive proteins MRTFA and YAP, and the suggested mechanism. **a** Immunofluorescent images of MRTFA stained cells grown on collagen I coated gels (60/40 % NIPAM/NEAM gel with AuNRs) that are present in the actuating area (340 mW power, 1 Hz, 100 ms laser ON time, top row) showing nuclear localisation and in the non-actuating area where MRTFA is in the cytoplasm. **b** Quantification of the nuclear percentage of MRTFA ($n = 3$, $N \geq 60$ cells). **c** Immunofluorescent images of cells grown on collagen I coated gels shows more aligned fibronectin secretion when cells are actuated, $n = 3$, $N \geq 211$ cells) (green = actin, blue = nucleus, scale bar = 20 μm). **d, e** Quantification of the fibronectin signal shows more fibronectin in the actuated region as well as more fibronectin production per cell by actuated cells. **f** A schematic depicting the suggested mechanism. When the hydrogel film actuates, cells experience forces that are transduced to the nucleus via F-actin filaments, formed by G-actin polymerisation. When G-actin is released to make F-actin, MRTFA translocates from the cytoplasm to the nucleus. Upon cessation of actuation, MRTFA returns back to the cytoplasm. YAP, on the other hand, does not show shuttling behaviour in response to actuation of this hydrogel film but is already present in the nucleus due to the stiffness of this gel (~30 kPa under cell culture conditions). In the box plots, the interquartile range (IQR) between the first and the third quartiles is indicated by the box, while whiskers denote 1.5 IQR. The hollow square, the horizontal line, and the filled dots represent the average, the median, and the outliers, respectively. *, **, *** are determined using one way ANOVA or Welch test, depending on the homogeneity of variances, and represent statistical significance at $p < 0.05$, 0.01 and 0.001, respectively

work, while above this threshold, the internal machinery may be unable to react to the fast time scale¹⁰. According to the molecular clutch model, focal adhesions are given the analogy of a molecular clutch. A clutch is engaged when the actin network is coupled to the ECM through integrin binding, resulting in the formation of focal adhesions⁴⁶. It has to break to enable cell migration. In the light of the mechanosensitive molecular clutch

model^{46,47}, more FAs observed on actuated cells correspond to more engaged clutches, which suggests talin unfolding succeeded by vinculin unfolding. As the gel modulus here is comparable to the talin unfolding threshold (~30 kPa, regarded as ‘stiff’ by the cell^{42,46}), the presence of more focal adhesions upon actuation, suggests a further enhancement of talin unfolding due to actuation. It is well known that on stiff substrates, engaged clutches

reach their breaking strength easily to facilitate cell migration. As less cell migration is observed on the actuating gels, it can be postulated that the rate of load transmission to the clutch is slowed down and the breaking strength is not reached as easily, although this hypothesis warrants further investigation in follow-up studies. Interestingly, more FAs are observed along the ridge edges, which are the sites of actuation.

This suggests the need for additional polymerisation of actin in response to the mechanical stresses experienced by the cells and corroborates with previous reports that MRTFA plays an important role between mechanical stresses and mechanotransduction to the nucleus. YAP, on the other hand, is unaffected by actuation and is always in the nucleus when the cell is sufficiently spread. The ‘nuclear pore’ theory provides a nexus between nuclear accumulation of proteins and substrate stiffness^{39,48}. Nuclear entry of protein molecules is promoted by nuclear flattening that leads to an enlargement of nuclear pores and depends on the 3D size of the protein. As nuclear flattening occurs when cells spread, this is greatly affected by substrate stiffness. At 36 °C, the present hydrogel film has a modulus of ~30 kPa, leading to nuclear pores that are sufficiently large for YAP (65 kDa), which is already mainly located in the nucleus on static gels. On the other hand, the larger protein MRTFA (160 kDa) only enters the nucleus upon actuation (Fig. 5). This suggests two possibilities: the nuclear pores are large enough before actuation to facilitate MRTFA entry or they undergo further enlargement during actuation. As no difference in cell spreading is observed between the actuated and the non-actuated gels, the first possibility is more likely.

Cells ‘feel’ the repetitive small deformations (~1.6–4 µm), which manifest in changes in focal adhesions and their migration rate, driven by intracellular molecular pathways. User-defined forces are locally exerted on gels and affect cell behaviour in a mechanobiological manner when applied for multiple hours, while gel topography, stiffness and surface coating can be independently varied. This allows for the identification of (disrupted) mechanosensor circuits, as mechanical forces are decoupled from the physical and biochemical environment of cells. To the best of our knowledge, this is the first system that can exert such stresses on a spatially selected cell population for a prolonged period of time.

Methods

Materials. N-isopropyl acrylamide (NIPAM, 97%), N-ethyl acrylamide (NEAM, 99%), photo-initiator (2-hydroxy-4-(2-hydroxyethoxy)-2-methylpropiophenone, 98%), crosslinker (N, N'-methylenebisacrylamide, 99%), acetone, isopropanol, 3-(trimethoxysilyl) propyl acrylate (92%) and dimethyl sulfoxide (DMSO) are purchased from Sigma–Aldrich. Fluorescent hydrogels are prepared by using fluorescein-o-acrylate (Sigma–Aldrich) or methacryloxyethyl thiocarbonyl rhodamine B (Polysciences) and moulds for compression test are made from poly(dimethylsiloxane) (PDMS, Sylgard 184, Dow Corning). All solvents are purchased from Sigma–Aldrich unless otherwise mentioned. Deionised water (0.1 µS/cm, ELGA Purelab-Plus), sodium borohydride (NaBH₄, 99%), cetyltrimethylammonium bromide (CTAB, 99%) hydrogen tetrachloroauric (III) acid (HAuCl₄), ascorbic acid (99%) silver nitrate (AgNO₃, 99.99%), chloroform are used for the production of gold nanorods. Thiol functionalised polyethylene glycol (PEG) polymer (HS-PEG-OH, Mw = 3000 Da, Iris Biotech) is used for the modification of the AuNRs. L929 mouse-derived fibroblasts are cultured in RPMI medium (Gibco), supplemented with 10% fetal bovine serum (FBS, Biowest) and 1% antibiotics/antimycotics (Gibco). Fibronectin from human plasma (Sigma–Aldrich, F2006) or Collagen 1 (Thermo Fisher A1064401) is dissolved in endotoxin-free water and used for coating the gels using sulfo-succinimidyl 6-(4'-azido-2'-nitrophenylamino)hexanoate (Sulfo-SANPAH) (Thermo Fisher 22589) as a covalent linker. The MTS (3-(4,5-dimethylthiazol-2-yl)-5-(3-carboxymethoxyphenyl)-2-(4-sulfophenyl)-2H-tetrazolium) assay (Promega G5421) is used to quantify the number of viable cells. Anti-mouse MRTFA primary antibody (Santacruz biotech, sc398675) is used at a dilution of (1:100), while anti-mouse Alexa Fluor 633 from Thermo Fisher (A 21050) is used as the secondary antibody, dilution 1:100. YAP primary antibody (Cell Signaling Technologies, 4912 S) is used at a dilution of 1:100 with anti-rabbit secondary AF 488 (Thermo Fisher, dilution 1:100). Cell nuclei are stained with DAPI (4',6-diamidino-2-phenylindole, while

the actin cytoskeleton is stained using cytopainter iFluor-594 (abcam ab 176757, dilution 1:400). Anti-fibronectin from rabbit (Sigma–Aldrich F3648), anti-paxillin from rabbit (Sigma–Aldrich SAB4502553) and anti-vinculin from mouse (Sigma–Aldrich V9264) is employed at a dilution of 1:100.

Preparation of hydrogels. The hydrogels are fabricated using a silicon mould template replication polymerisation technique. Since free-standing thin gels do not retain their shape, gel films are tethered to a glass coverslip silanised with (3-(trimethoxysilyl) propyl acrylate silane) (Supplementary Method 1). Hydrogels are fabricated by co-polymerisation of N-isopropyl acrylamide (NIPAM) and N-ethyl acrylamide (NEAM). NIPAM is recrystallised from hexane and NEAM is passed through a neutral alumina column before use. A polymer precursor solution, which contains the monomers NIPAM and NEAM, crosslinker and initiator in DMSO forms a thin film between an acryl silanised coverslip and a microstructured silicon wafer with continuous grooves and ridges, both 25 µm wide and 2.7 µm deep (Supplementary Fig. 1, 2, Supplementary Note 1). To obtain a VPTT near the physiological temperature of 37 °C, hydrogels with different ratios of NIPAM (LCST ~32 °C) and NEAM (LCST 82 °C)⁴⁹ are prepared. The molar ratios of NIPAM and NEAM are varied from 100/0, 70/30, 60/40, 50/50 and 0/100 mole % NIPAM/NEAM to vary the volume phase transition temperature (VPTT) of the gel. For a 60/40 molar ratio of NIPAM/NEAM, 0.2 g NIPAM and 0.12 g NEAM is added to 333 µL DMSO along with 6.6 mg photo-initiator (Irgacure 2959) and 4.5 mg crosslinker (N,N'-methylenebisacrylamide, BIS), resulting in a VPTT around the physiological temperature (37 °C). Upon UV polymerisation, a thin gel film is covalently attached to the modified glass coverslip. The VPTTs are determined by measuring the dimensions of the ridge widths on the gels in the presence of cell culture medium and defined as the inflection point of the sigmoid curve. PEG-functionalised gold nanorods (AuNRs) in DMSO are added in such a way that an optical density (OD) of ~95 with a AuNR number density 3.6/µm³ is achieved at a wavelength of 808 nm for a path length of 1 cm. The amount of DMSO is compensated to account for the AuNRs added and achieve a gel precursor solution at ~57 w/v % monomer.

Fabrication of patterned or flat hydrogels is performed in the glovebox in a low oxygen environment (<0.40%). Drops of gel precursor solution (1.5 µL each) are placed on top of the silicon wafer and an acryl silanised coverslip is placed on top of the drop such that the precursor solution is present in the interspace between the silicon wafer and the coverslip.

The gels are cured for 30 min under UV light (Konrad Benda lamp 366 & 254 nm, 8 W). After curing, they are immersed overnight in excess de-ionised water at ~25 °C to remove DMSO. This facilitates hydrogel swelling and easy peeling of the gels from the patterned silicon surface. Fluorescent hydrogels are prepared by adding 0.4 mg fluorescein-o-acrylate or methacryloxyethyl thiocarbonyl rhodamine B (Polysciences Inc) in 100 µL of the gel precursor solution. The gels are washed thrice with excess DMSO to remove the unreacted monomers and then thrice with Milli Q water. The gels are sterilised in 70% ethanol for 30 min and washed with water thrice. Surface functionalisation of the gels with fibronectin is used for all photothermal analysis in this study, except for AFM measurements and ridge width analysis at thermal equilibrium for different temperatures to determine the VPTT.

Synthesis and modification of AuNRs. AuNRs are synthesised by a seed-mediated growth method, as reported elsewhere^{31,50,51}. A fresh seed solution is prepared by adding 0.60 ml of an aqueous ice-cold 0.010 M NaBH₄ to a mixture of water (4.2 mL), 0.20 M CTAB (5.0 mL) and 0.0030 M HAuCl₄ (0.83 mL) under vigorous stirring for 2 min. The growth solution is prepared by adding a mixture of 0.20 M CTAB (150 mL), 0.050 M ascorbic acid (3.1 mL) and 0.0080 M AgNO₃ (3.3 mL) to 0.0010 M HAuCl₄ (150 mL). 0.875 mL of seed solution is added to the growth solution at 25 °C in a water bath and stirred vigorously for 30 min. This is followed by the addition of 0.050 M ascorbic acid (2.0 mL) at a flow rate of 0.50 mL/h and stirring for another 30 min. The resultant brownish red solution containing AuNRs is centrifuged at 10,492 × g for 25 min in a centrifuge (Heraeus Multifuge X3R). The AuNRs that precipitate are resuspended in 2 mL water (0.1 µS/cm, ELGA Purelab-Plus), while the supernatant containing excess surfactant is discarded.

A 10 mL solution of the AuNRs, prepared as above, is re-dispersed in 100 mL water and mixed with 20 mL solution of 2.5 mM thiol functional PEG (HS-PEG-OH, Mw = 3000 Da, Iris Biotech) in ethanol under stirring. This solution is sonicated at 60 °C for 30 min and subsequently for another 3.5 h at 20 °C. The solution is stirred overnight and then extracted with chloroform thrice (~120 mL) to remove CTAB and free polymer. In a second purification step, the AuNRs are transferred to 25 mL DMSO and centrifuged at 9416 × g for 20 min. The supernatant is discarded and the solution containing concentrated AuNRs (2 mL) is diluted with DMSO and centrifuged three times. After the last centrifugation, the concentrated AuNR dispersion in DMSO is used for further experiments. The modified AuNRs have a longitudinal surface plasmon resonance at λ = 795 nm (UV-Vis spectrum, V-630, JASCO). They have an average length of 70 nm, width of 16 nm, and aspect ratio of ~4.4. The amount of AuNRs is quantified (Supplementary Method 2) and pre-mixed at a specific concentration (3.6 AuNRs/µm³) in the gel precursor solution before polymerisation.

Determination of the volume phase transition temperature (VPTT). The VPTT of non-surface functionalised gels is analysed by measuring the widths of the patterns in response to changes in temperature (Fig. 1). The patterned gels are placed inside a custom-made PDMS mold that is filled with cell culture medium and put on a Peltier stage, fixed to an optical microscope (Keyence, VHZ 100UR). A small temperature sensor (Pt, K100) is connected to a Keithley resistor and is used to measure and record the temperature of the medium at an interval of 1 s. Micrographs are captured after the gel is allowed to equilibrate for at least 15 min at different temperatures and analysed using ImageJ software. The ridge widths are calculated from the plot profiles.

Laser actuation setup and exposure conditions. A custom-made setup, which can simultaneously irradiate the gels at the required wavelength, as well as observe the gel and cells, is designed to perform the experiments (Supplementary Fig. 10, Supplementary Method 3). The laser is mounted on an inverted microscope and focussed on the gel through a collimator. A port on the microscope (Zeiss Axiovert 100) is especially modified to connect a diode laser (λ_{\max} 808 nm, maximum power 340 mW, Roithner Lasertechnik) through a fibre optic cable, while a collimator is used to focus the laser beam on the sample (footprint area ~ 1.2 mm², major axis ~ 1.9 mm, minor axis 0.83 mm). An incubator chamber around the microscope ensures that standard cell culture conditions are maintained. The gels are mounted on a custom-designed sample holder, Supplementary Method 3). A low pass IR filter (Edmund Optics) is added in the optical path to prevent the IR light from reaching the high-speed camera (Hamamatsu ORCA-Flash 4.0 CMOS). The laser power reaching the gel is experimentally measured using a power meter (Thor Labs PM 400) and the intensity is calculated from the spot size observed on the gel. The laser footprint on the gel is kept the same for all experiments. Different laser settings are applied (Table 1) and an Arduino circuit is used as a variable trigger to control the laser. Brightfield images of the gels are acquired at a rate (10–100 fps) when the laser is pulsing. The actuation amplitude is determined as the maximum difference in ridge width during actuation using Image J software. The actuated region of the gel is identified using grid markings and all cells growing in the actuated zone are considered for analysis. Cells growing at least 200 μ m away from the actuated regions are chosen randomly as control cells.

Temperature measurements. An IR thermal imaging camera (FLIR A655 sc) is employed to measure the temperature changes due to photothermal heating (Supplementary Fig. 7a). For this purpose, the gel is sealed with cell culture medium in a secure seal spacer (Electron Microscopy Sciences, 70327) with glass coverslips (Marienfeld, 1.5 H) on both sides and is placed on top of a Peltier stage. The laser is incident obliquely from the top. Prior to measuring samples, the thermal camera is calibrated before the measurement using a pre-calibrated Peltier stage, whose temperature is set at 30 °C (lower limit) and 43 °C (upper limit), the emissivity value is set at 0.98. The IR camera is calibrated assuming a linear fit between the radiance values at the upper and lower limit temperatures between which the calibration is valid. The thermal images are recorded at a speed of 50 fps before (0–60 s), during (61–120 s) and after pulsing (121–160 s). Gels are pulsed with a frequency of 1 Hz, ON time of 100 ms, and 340 mW laser power. The temperature changes for control gels (0/100 NIPAM/NEAM gel with AuNRs and 60/40 NIPAM/NEAM gels without AuNRs) are measured in a similar way.

Simulation of heat dissipation in response to NIR laser. The heat distribution, generated by the AuNRs in response to the incident light, is simulated using the FREE FEM ++ (v. 3.610001) software⁵². In this simplified model, the assumption is made that heat transfer is dominated by heat conduction, and that convection and radiation are negligible. The heat equation for the simulated volume of the hydrogel film and media is solved using the finite element method (Supplementary Note 5 for details).

Cell culture and actuation. Cell culture experiments are performed with L929 mouse-derived fibroblasts (Deutsche Sammlung von Mikroorganismen und Zellkulturen GmbH, DSMZ ACC-2). Fibroblasts are cultured in RPMI medium with 10% FBS and 1% antibiotics/antimycotics at 37 °C, 5% CO₂ and 95% humidity. The gel surface is modified with fibronectin or collagen I using sulfo-SANPAH as a bi-functional crosslinker (Supplementary Method 4).

Cells are seeded on the fibronectin functionalised gels at a seeding density of $\sim 30,000$ cells/gel. After allowing cells to adhere for 8–24 h, the gels are actuated for different periods between 1 and 22 h. The gels are placed in a custom-made cell chamber and at least three gels are studied per condition (Supplementary Fig. 10).

Analysis of cell motility. Time-lapse microscopy at 1 h intervals is performed to monitor the effect of gel actuation on cell motility using Cell Tracker⁵³ software to analyse at least 44 cells per condition. Cells that fulfil the following criteria are randomly selected:

- Cells do not divide during imaging;
- Cells are not positioned at the borders of the field of view of the image (as they tend to go out of the field of view over time).

Afterwards, cell nuclei are assigned to an x–y coordinate system and tracked using the semi-automatic mode and template matching modality. Once all trajectories are obtained and examined, different parameters, such as end-to-end distance, contour length, persistence length, projected contour length and cell migration rate are computed (Supplementary Method 5, Supplementary Note 7).

Microscopy. Laser scanning confocal microscopy is performed with a Leica SP 8 Tandem Confocal microscope using a white light laser for excitation. Suitable excitation and emission filters are applied. All imaging involving cells are performed at 37 °C to avoid excessive swelling of the hydrogels. The thickness of the hydrogels at different temperatures is determined by acquiring images in the z-stacking mode. Sequential scanning is performed to avoid cross-talk between channels. Super resolution confocal images are acquired using the stimulated emission depletion (STED) technique. A pulsed laser at 775 nm is used for depleting the fluorescence excitation. The point spread function is regulated using an in plane (xy) and a z component of the de-excitation laser. The detector is set in counting mode while imaging Elf, Hsp 70 and fibronectin. Image deconvolution is performed with Huygens Professional software (Scientific Volume Imaging B.V.) Confocal micrographs of immunostained cells are analysed using ImageJ (Fiji, version 1.52b) to quantify the nuclear MRTFA (%), focal adhesions, fibronectin secreted by cells and the levels of Hsp 70 and Elf in the cells (Supplementary Method 6). For each condition, $N \geq 60$ cells are pooled from three independent experiments and analysed, unless otherwise mentioned.

Mechanical properties. The 60/40 NIPAM/NEAM gels are subjected to monotonic compression at different temperatures to investigate the change in elastic moduli of the bulk gel below and above the VPTT. For this purpose, gels are prepared in circular PDMS moulds of 10 mm diameter and 1 mm height. The moulds are attached to a clean glass slide using silicon grease and 70 μ L of the gel precursor solution is added to each well such that the well is filled up to the brim. A glass coverslip is placed on top of every well to obtain a flat surface and avoid evaporation and the precursor solution is subjected to UV polymerisation as described earlier. After curing, the gels are washed overnight with DI water and equilibrated with cell culture media at the required temperature overnight. An immersion chamber of the dynamic mechanical analyser (TA instruments) is used to completely submerge the sample in cell culture medium during the measurements. A pre-load force of 0.001 N and a cross-head speed of 0.05 N/min is applied to compress the gels until a force of 0.5 N is reached. At least three different samples are evaluated at each temperature. The stress is determined using the surface area of the gels, determined via the swelling measurements performed at different temperatures (Supplementary Method 7). The stress-strain curves are analysed and the bulk compressive modulus of the gels is determined as the initial slope of the curve up to 5% strain.

The local mechanical properties of the hydrogels are determined by the Young modulus of the gels via atomic force microscopy (Bruker Dimension Icon AFM, colloidal probe with an A-shaped cantilever, CP-PNPS-B from Nano and More). The probe is a silica bead with a radius of ~ 3.31 μ m and spring constant of ~ 0.21 N/m, determined by thermal calibration. Samples are indented using a maximal force (relative set point) of 2 nN at three different temperatures (27, 37 and 45 °C) on a 5 \times 5 raster pattern with 100 nm step size. At least 4 different areas are measured in this method to screen at least 100 points per condition. The elastic modulus, E, is obtained from the force-indentation curves using a Hertz model with the contact point as free parameter. The Poisson ratio is assumed to be 0.5.

Table 1 Experimental parameters used for actuation

Parameter	Experimental conditions varied	Experimental conditions kept constant
Time of actuation (h)	0, 4, 8, 12, 22	@ 340 mW, 1 Hz, 100 ms laser ON time
Laser Pulse (ms)	0, 20, 100	@ 340 mW, 1 Hz, 12 h laser exposure
Laser output (mW)	0, 100, 260, 340	@ 1 Hz, 100 ms laser ON time, 12 h laser exposure
Frequency (Hz)	1, 0.5, 0.1	@ 340 mW, 100 ms laser ON time, 12 h laser exposure
Frequency (Hz)	1, 5, 10	@ 340 mW, 20 ms laser ON time, 12 h laser exposure
Relaxation (h)	0, 2.5, 5, 10, 14	After laser exposure @ 340 mW, 100 ms laser ON time, 12 h laser exposure

Statistical analysis. Statistical analyses are performed using IBM SPSS Statistics 20 software. Values are presented as mean \pm standard deviation, unless otherwise mentioned. Error bars represent standard deviation. Data are analysed with a one way ANOVA and post-hoc Tukey test when homogeneity of variances (determined by Levene's test) is valid and a Welch test with post-hoc Games Howell test when homogeneity of variances is not obeyed with statistical significance defined at $p < 0.05$, 0.01 and 0.001, represented by *, ** and *** respectively.

Reporting summary. Further information on research design is available in the Nature Research Reporting Summary linked to this article.

Data availability

The authors declare that (the/all other) data supporting the findings of this study are available within the paper and its supplementary information files or from the corresponding authors upon reasonable request.

Received: 7 November 2018 Accepted: 11 July 2019

Published online: 06 September 2019

References

- King, N. Nature and nurture in the evolution of cell biology. *Mol. Biol. Cell* **21**, 3801–3802 (2010).
- Vogel, V. & Sheetz, M. Local force and geometry sensing regulate cell functions. *Nat. Rev. Mol. Cell Biol.* **7**, 265 (2006).
- Alam, S., Lovett, D. B., Dickinson, R. B., Roux, K. J. & Lele, T. P. in *Progress in Molecular Biology and Translational Science*. Vol. 126, 205–215 (Elsevier, 2014).
- Wang, J. H. C. & Thampatty, B. P. An introductory review of cell mechanobiology. *Biomech. Model. Mechanobiol.* **5**, 1–16 (2006).
- Huang, H., Kamm, R. D. & Lee, R. T. Cell mechanics and mechanotransduction: pathways, probes, and physiology. *Am. J. Physiol.-Cell Physiol.* **287**, C1–C11 (2004).
- Fabry, B., Maksym, G. N., Hubmayr, R. D., Butler, J. P. & Fredberg, J. J. Implications of heterogeneous bead behavior on cell mechanical properties measured with magnetic twisting cytometry. *J. Magn. Magn. Mater.* **194**, 120–125 (1999).
- Iskratsch, T., Wolfenson, H. & Sheetz, M. P. Appreciating force and shape—the rise of mechanotransduction in cell biology. *Nat. Rev. Mol. Cell Biol.* **15**, 825 (2014).
- Rodriguez, M. L., McGarry, P. J. & Sniadecki, N. J. Review on cell mechanics: experimental and modeling approaches. *Appl. Mech. Rev.* **65**, 060801 (2013).
- Luo, T., Mohan, K., Iglesias, P. A. & Robinson, D. N. Molecular mechanisms of cellular mechanosensing. *Nat. Mater.* **12**, 1064 (2013).
- Jungbauer, S., Gao, H., Spatz, J. P. & Kemkemer, R. Two characteristic regimes in frequency-dependent dynamic reorientation of fibroblasts on cyclically stretched substrates. *Biophys. J.* **95**, 3470–3478 (2008).
- Camelliti, P., Gallagher, J. O., Kohl, P. & McCulloch, A. D. Micropatterned cell cultures on elastic membranes as an in vitro model of myocardium. *Nat. Protoc.* **1**, 1379 (2006).
- Cui, Y. et al. Cyclic stretching of soft substrates induces spreading and growth. *Nat. Commun.* **6**, 6333 (2015).
- Sutton, A. et al. Photothermally triggered actuation of hybrid materials as a new platform for in vitro cell manipulation. *Nat. Commun.* **8**, 14700 (2017).
- Engler, A. J., Sen, S., Sweeney, H. L. & Discher, D. E. Matrix elasticity directs stem cell lineage specification. *Cell* **126**, 677–689 (2006).
- Rose, J. C. et al. Nerve cells decide to orient inside an injectable hydrogel with minimal structural guidance. *Nano Lett.* **17**, 3782–3791 (2017).
- Omidinia-Anarkoli, A. et al. An injectable hybrid hydrogel with oriented short fibers induces unidirectional growth of functional nerve cells. *Small* **13**, 1702207 (2017).
- Rose, J. C. et al. Biofunctionalized aligned microgels provide 3D cell guidance to mimic complex tissue matrices. *Biomaterials* **163**, 128–141 (2018).
- Rosales, A. M. & Anseth, K. S. The design of reversible hydrogels to capture extracellular matrix dynamics. *Nat. Rev. Mater.* **1**, 15012 (2016).
- Kloxin, A. M., Kasko, A. M., Salinas, C. N. & Anseth, K. S. Photodegradable hydrogels for dynamic tuning of physical and chemical properties. *Science* **324**, 59–63 (2009).
- Yang, C., Tibbitt, M. W., Basta, L. & Anseth, K. S. Mechanical memory and dosing influence stem cell fate. *Nat. Mater.* **13**, 645 (2014).
- Guvendiren, M. & Burdick, J. A. Stiffening hydrogels to probe short- and long-term cellular responses to dynamic mechanics. *Nat. Commun.* **3**, 792 (2012).
- Gillette, B. M., Jensen, J. A., Wang, M., Tchao, J. & Sia, S. K. Dynamic hydrogels: switching of 3D microenvironments using two-component naturally derived extracellular matrices. *Adv. Mater.* **22**, 686–691 (2010).
- Lin, D. C., Yurke, B. & Langrana, N. A. Mechanical properties of a reversible, DNA-crosslinked polyacrylamide hydrogel. *J. Biomech. Eng.* **126**, 104–110 (2004).
- Rammensee, S., Kang, M. S., Georgiou, K., Kumar, S. & Schaffer, D. V. Dynamics of mechanosensitive neural stem cell differentiation. *Stem Cells* **35**, 497–506 (2017).
- Stowers, R. S., Allen, S. C. & Suggs, L. J. Dynamic phototuning of 3D hydrogel stiffness. *Proc. Natl. Acad. Sci.* **112**, 1953–1958 (2015).
- Liu, L. et al. Cyclic stiffness modulation of cell-laden protein–polymer hydrogels in response to user-specified stimuli including light. *Adv. Biosyst.* **2**, 1800240 (2018).
- Rosales, A. M., Mabry, K. M., Nehls, E. M. & Anseth, K. S. Photoresponsive elastic properties of azobenzene-containing poly (ethylene-glycol)-based hydrogels. *Biomacromolecules* **16**, 798–806 (2015).
- Hörner, M. et al. Phytochrome-based extracellular matrix with reversibly tunable mechanical properties. *Adv. Mater.* **31**, 1806727 (2019).
- Kong, N., Peng, Q. & Li, H. Rationally designed dynamic protein hydrogels with reversibly tunable mechanical properties. *Adv. Funct. Mater.* **24**, 7310–7317 (2014).
- Kim, J., Yoon, J. & Hayward, R. C. Dynamic display of biomolecular patterns through an elastic creasing instability of stimuli-responsive hydrogels. *Nat. Mater.* **9**, 159 (2010).
- Mourran, A., Zhang, H., Vinokur, R. & Möller, M. Soft microrobots employing nonequilibrium actuation via plasmonic heating. *Adv. Mater.* **29**, 1604825 (2017).
- Anderson, R. R. & Parrish, J. A. Selective photothermolysis: precise microsurgery by selective absorption of pulsed radiation. *Science* **220**, 524–527 (1983).
- Song, A. S., Najjar, A. M. & Diller, K. R. Thermally induced apoptosis, necrosis, and heat shock protein expression in three-dimensional culture. *J. Biomech. Eng.* **136**, 071006-1–071006-10 (2014).
- Anderson, P. & Kedersha, N. Stress granules: the Tao of RNA triage. *Trends Biochem. Sci.* **33**, 141–150 (2008).
- Olson, E. N. & Nordheim, A. Linking actin dynamics and gene transcription to drive cellular motile functions. *Nat. Rev. Mol. Cell Biol.* **11**, 353 (2010).
- Foster, C. T., Gualdrini, F. & Treisman, R. Mutual dependence of the MRTF–SRF and YAP–TEAD pathways in cancer-associated fibroblasts is indirect and mediated by cytoskeletal dynamics. *Genes Dev.* **31**, 2361–2375 (2017).
- Parmacek, M. S. Myocardin related transcription factor A: mending a broken heart. *Circ. Res.* **107**, 168–170 (2010).
- Panciera, T., Azzolin, L., Cordenonsi, M. & Piccolo, S. Mechanobiology of YAP and TAZ in physiology and disease. *Nat. Rev. Mol. Cell Biol.* **18**, 758 (2017).
- Elosegui-Artola, A. et al. Force triggers YAP nuclear entry by regulating transport across nuclear pores. *Cell* **171**, 1397–1410.e1314 (2017).
- Fiore, V. F. et al. $\alpha v \beta 3$ Integrin drives fibroblast contraction and strain stiffening of soft provisional matrix during progressive fibrosis. *JCI Insight* **3**, 97597 (2018).
- Kishi, T., Mayanagi, T., Iwabuchi, S., Akasaka, T. & Sobue, K. Myocardin-related transcription factor A (MRTF-A) activity-dependent cell adhesion is correlated to focal adhesion kinase (FAK) activity. *Oncotarget* **7**, 72113 (2016).
- Elosegui-Artola, A. et al. Mechanical regulation of a molecular clutch defines force transmission and transduction in response to matrix rigidity. *Nat. Cell Biol.* **18**, 540 (2016).
- Li, C. X. et al. MicroRNA-21 preserves the fibrotic mechanical memory of mesenchymal stem cells. *Nat. Mater.* **16**, 379 (2017).
- Ehrbar, M. et al. Biomolecular hydrogels formed and degraded via site-specific enzymatic reactions. *Biomacromolecules* **8**, 3000–3007 (2007).
- Qin, Z. & Bischof, J. C. Thermophysical and biological responses of gold nanoparticle laser heating. *Chem. Soc. Rev.* **41**, 1191–1217 (2012).
- Swaminathan, V. & Waterman, C. M. The molecular clutch model for mechanotransduction evolves. *Nat. Cell Biol.* **18**, 459 (2016).
- Humphries, J. D. et al. Vinculin controls focal adhesion formation by direct interactions with talin and actin. *J. Cell Biol.* **179**, 1043–1057 (2007).
- Strzyz, P. Enforcing protein import. *Nat. Rev. Mol. Cell Biol.* **18**, 713 (2017).
- Wang, Q. et al. Random copolymer gels of N-isopropylacrylamide and N-ethylacrylamide: effect of synthesis solvent compositions on their properties. *RSC Adv.* **7**, 9381–9392 (2017).
- Jana, N. R., Gearheart, L. & Murphy, C. J. Seed-mediated growth approach for shape-controlled synthesis of spheroidal and rod-like gold nanoparticles using a surfactant template. *Adv. Mater.* **13**, 1389 (2001).
- Bartneck, M. et al. Rapid uptake of gold nanorods by primary human blood phagocytes and immunomodulatory effects of surface chemistry. *ACS Nano* **4**, 3073–3086 (2010).
- Hecht, F. New development in FreeFem++. *J. Numer. Math.* **20**, 251–266 (2012).

53. Piccinini, F., Kiss, A. & Horvath, P. Cell tracker (not only) for dummies. *Bioinformatics* <https://doi.org/10.1093/bioinformatics/btv686> (2015).

Acknowledgements

We thank Prof. Joachim Spatz for providing inspiration for this project, R. Vinokur, S. Moli, C. Bastard and S. Babu for their help with the experiments and J. Di Russo for discussions. We acknowledge funding from the Deutsche Forschungsgemeinschaft (grant LA 3606/2-1) and European Union's Horizon 2020 research and innovation program under the Marie Skłodowska-Curie grant agreement No 642687, and M.M. acknowledges support from the ERC Advanced Grant 695716. This work is performed in part at the Center for Chemical Polymer Technology (CPT), which is supported by the EU and the federal state of North Rhine-Westphalia (grant EFRE 30 00 883 02). Financial support from the European Commission (EUSMI, 731019) and DFG GRK 2415, 363055819 is also acknowledged.

Author contributions

Y.C. developed the platform to actuate cells on hydrogel films, fabricated and characterised the hydrogel and performed all the NIR cell actuation experiments and analysis and wrote the manuscript. A.C.N. fabricated the gels and performed the mechanical characterisation experiments and cell proliferation assays. Y.C., A.C.N. and T.H. analysed cell migration, while Y.C. and R.W. analysed focal adhesions. S.S. developed the protocol for production of AuNRs. M.V.D. helped with the NIR experiments. T.H. performed the AFM experiments, simulation experiments and provided intellectual contribution. H.Z. and J.K. performed preliminary testing of the effect of NEAM as a co-monomer to change the VPTT. A.M. helped supervising the project and provided intellectual contribution. M.M. and A.M. developed light-responsive PNIPAM gels with incorporated AuNRs. Inspired by this technology, L.D.L. translated the concept to actuate living cells for prolonged duration, secured funding for the project, supervised the project and wrote the manuscript.

Additional information

Supplementary Information accompanies this paper at <https://doi.org/10.1038/s41467-019-11475-4>.

Competing interests: The authors declare no competing interests.

Reprints and permission information is available online at <http://npg.nature.com/reprintsandpermissions/>

Peer review information: *Nature Communications* would like to thank Florian Stadler and other, anonymous, reviewers for their contributions to the peer review of this work.

Publisher's note: Springer Nature remains neutral with regard to jurisdictional claims in published maps and institutional affiliations.



Open Access This article is licensed under a Creative Commons Attribution 4.0 International License, which permits use, sharing, adaptation, distribution and reproduction in any medium or format, as long as you give appropriate credit to the original author(s) and the source, provide a link to the Creative Commons license, and indicate if changes were made. The images or other third party material in this article are included in the article's Creative Commons license, unless indicated otherwise in a credit line to the material. If material is not included in the article's Creative Commons license and your intended use is not permitted by statutory regulation or exceeds the permitted use, you will need to obtain permission directly from the copyright holder. To view a copy of this license, visit <http://creativecommons.org/licenses/by/4.0/>.

© The Author(s) 2019

Supplementary information

Cellular responses to beating hydrogels to investigate mechanotransduction

Yashoda Chandorkar¹, Arturo Castro Nava¹, Sjören Schweizerhof¹, Marcel Van Dongen¹, Tamás Haraszti¹, Jens Köhler¹, Hang Zhang¹, Reinhard Windoffer², Ahmed Mourran¹, Martin Möller¹, Laura De Laporte,^{1,3*}

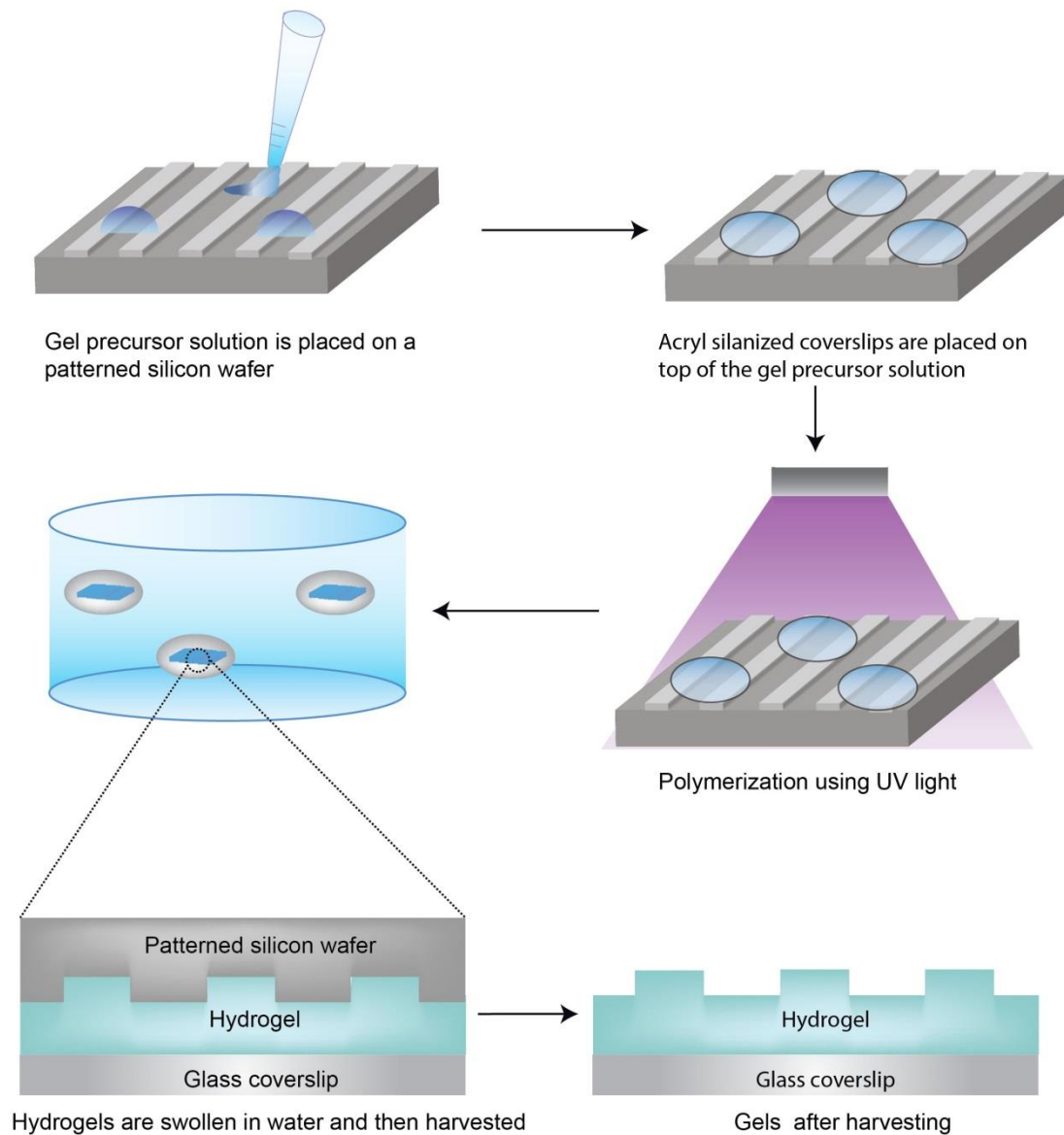
¹DWI – Leibniz-Institut für Interaktive Materialien e.V. Forckenbeckstr. 50, Aachen, 52074, Germany.

²Institute of Molecular and Cellular Anatomy, Uniklinik, RWTH Aachen University, Aachen, 52074, Germany.

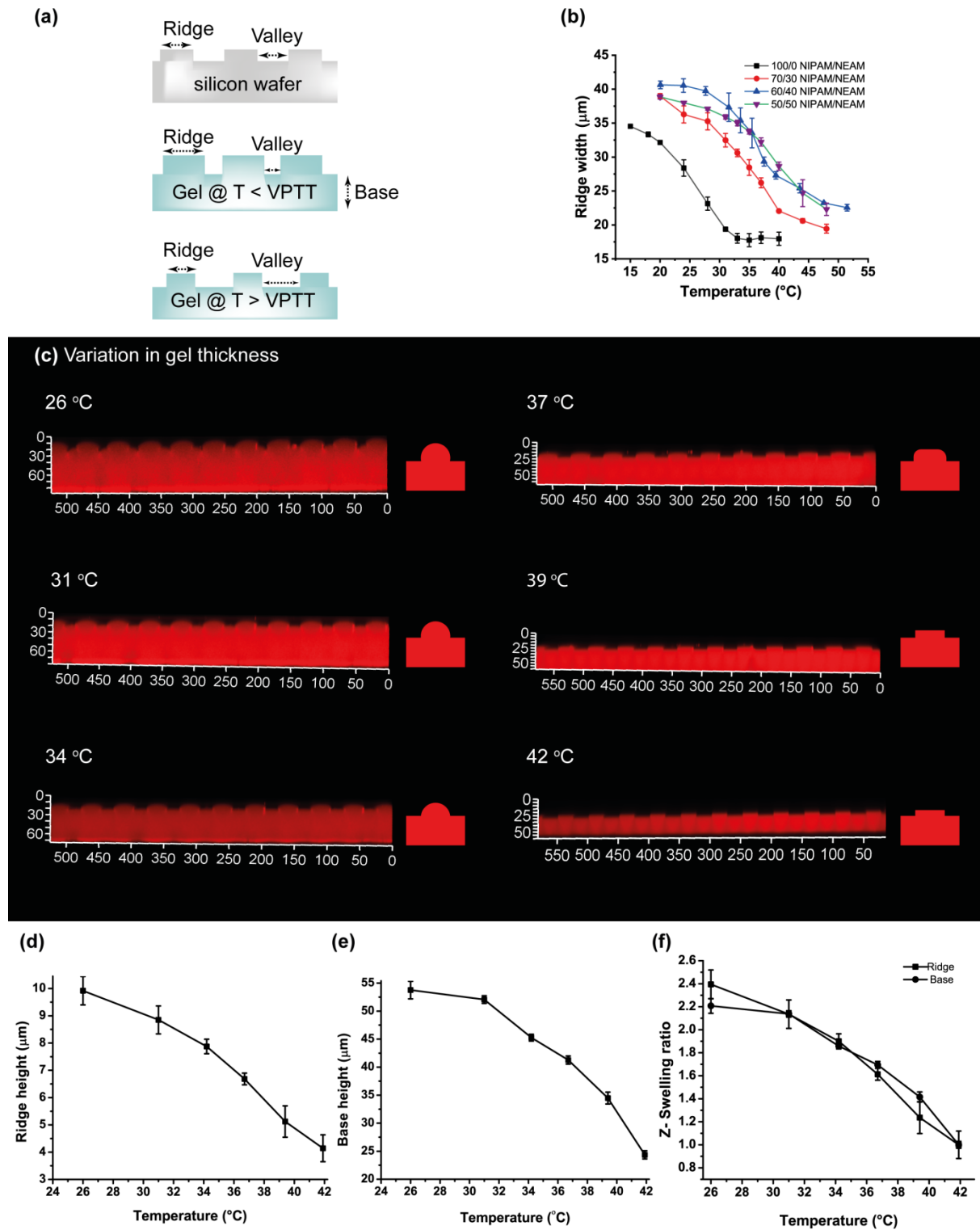
³ITMC- Institute of Technical and Macromolecular Chemistry, RWTH Aachen University, Aachen, 52074, Germany.

* Corresponding author

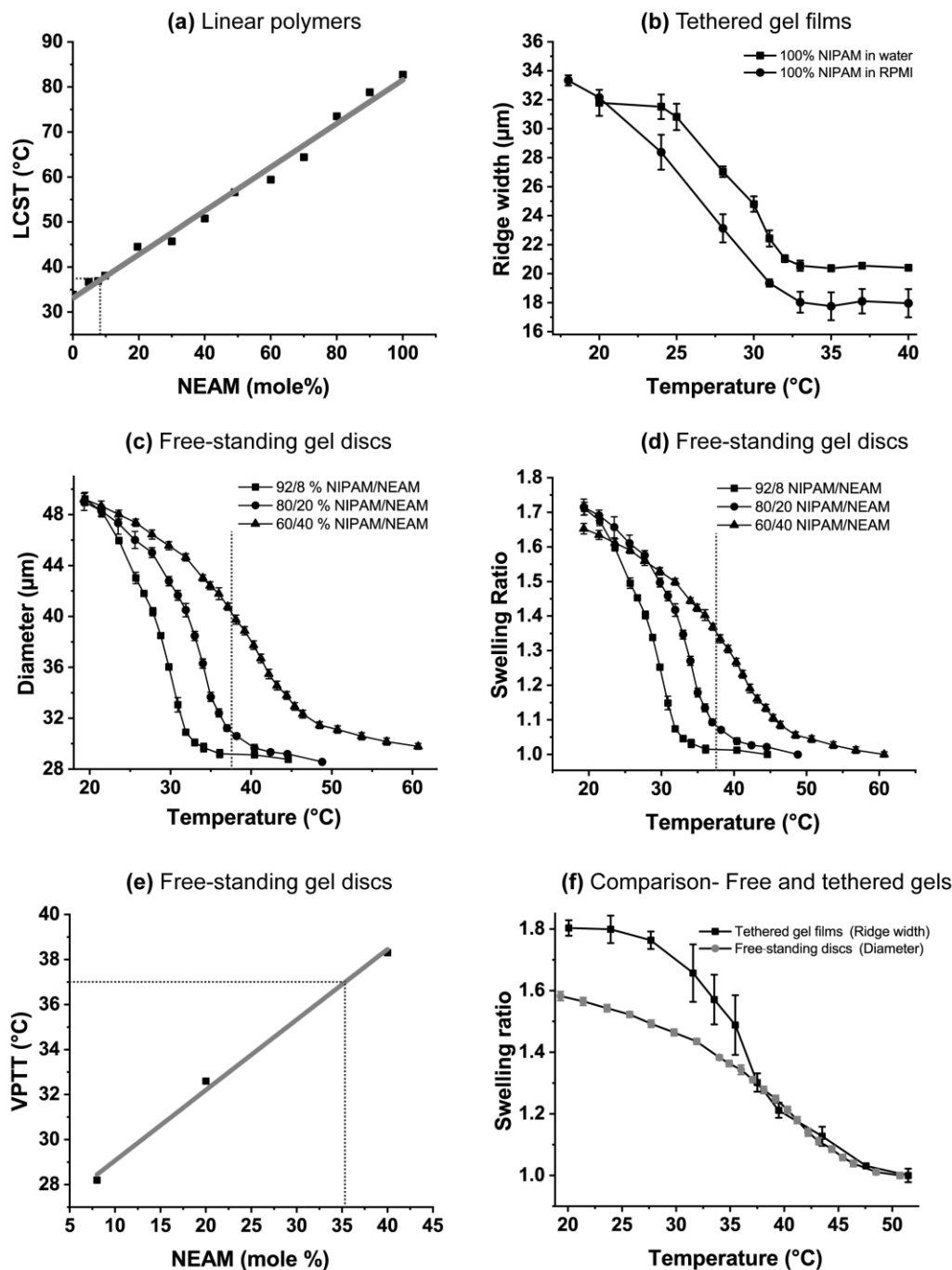
Supplementary Figures



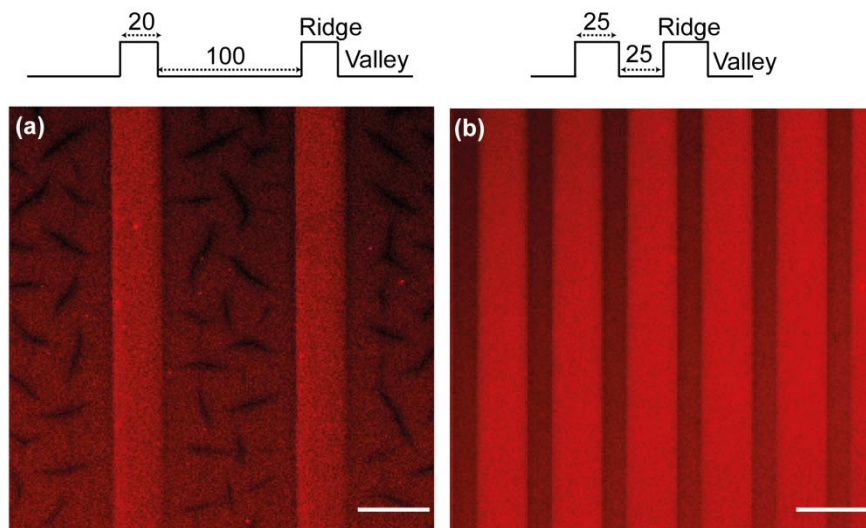
Supplementary Figure 1. Schematic showing the process of gel fabrication from the precursor solution using a silicon mould replication technique. Multiple drops of $1.5 \mu\text{l}$ gel precursor solution are placed on a silicon wafer with the desired microstructure. Acryl silanized glass coverslips are placed on top of each drop to form a thin sheet of the gel precursor solution, sandwiched between the glass coverslip and the silicon wafer. The gels are polymerized with UV light and swollen in excess deionized water overnight before harvesting.



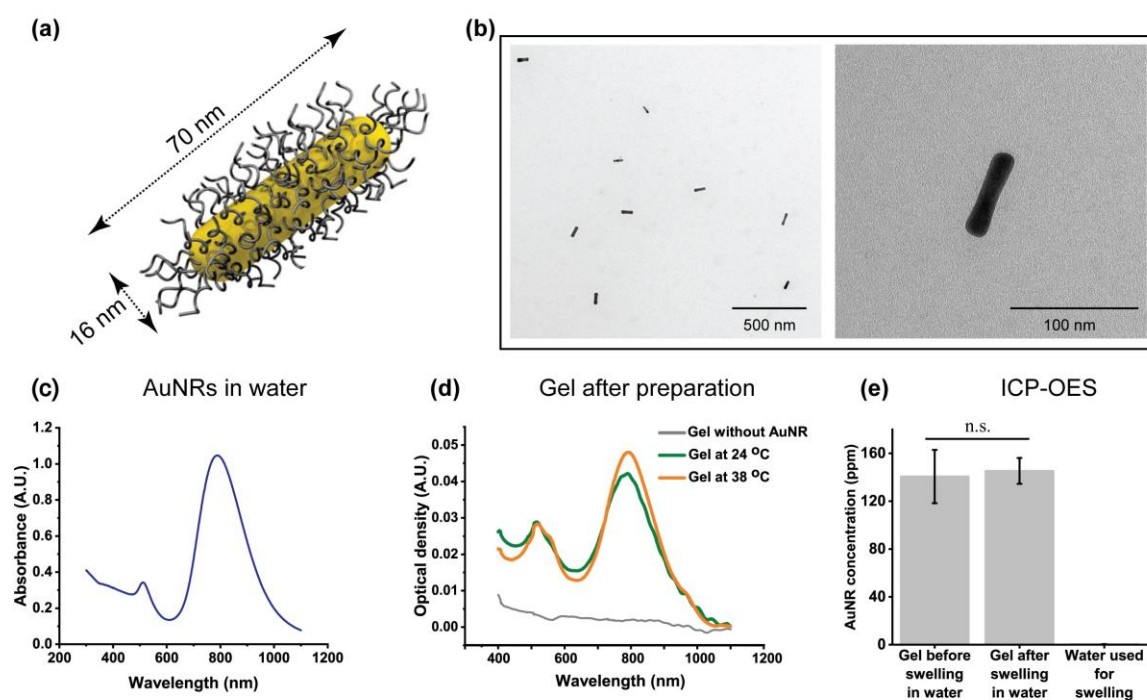
Supplementary Figure 2. (a) Schematic of the side views of the silicon wafer and the gels above and below the VPTT. The pattern on the silicon wafer has a depth of 2.7 μm . (b) The ridge widths at different temperatures plotted for crosslinked NIPAM/NEAM copolymers at different molar ratios (100/0 %, 70/30 %, 60/40 %, 50/50 %) to study the volume phase transition characteristics of the gel. A composition of 60/40 % NIPAM/NEAM exhibits a VPTT of ~ 37 $^{\circ}\text{C}$ and is used in this study, $n = 3$. (c) The z-stacked confocal images showing the thickness of the gel at 26, 31, 34, 37, 39, and 42 $^{\circ}\text{C}$. The hydrogel is confined as it is bound to a glass coverslip. The changes in the shape of the hydrogel and ridges are depicted in the illustrations. (d) The ridge height and (e) the base height, as determined from (c), vary with temperature. (f) The axial swelling ratios for the ridge and the base height are similar, suggesting isotropic actuation. Error bars represent standard deviation.



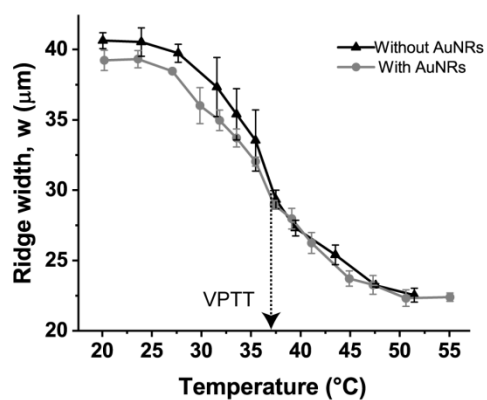
Supplementary Figure 3. (a) When linear polymers with different NIPAM/NEAM ratios are prepared using free radical polymerization and their LCST is measured in water using the cloud point method, a composition of 92/8 % NIPAM/NEAM shows an LCST of ~ 37 °C. (b) The VPTT of crosslinked 100 % NIPAM gels tethered to a glass coverslip (as used in the present study) is measured in water and RPMI cell culture medium to be ~ 28.8 °C and ~ 25.0 °C, respectively, demonstrating a significant decrease upon crosslinking and in the presence of media (LCST of non-crosslinked NIPAM in water is ~ 32 °C) (c) Diameter of free-standing gel discs, prepared with different copolymer ratios in a mould with a diameter of 30 µm and a height of 5 µm, at different temperatures in cell culture medium. (d) The swelling ratio of the discs obtained from the measurements in (c). (e) A linear dependence of the VPTT with the NEAM % is observed for the free-standing discs, where a 65/35 mole % NIPAM/NEAM shows a VPTT of ~ 36 °C. This is similar to the linear dependence obtained for tethered gels (used in the present study), where 60/40 mole % NIPAM/NEAM gels have a VPTT of ~ 36 °C, shown in Figure 1c (f) A comparison of the swelling ratios of tethered 60/40 NIPAM/NEAM gels films and free-standing discs, showing similar behaviour, suggesting that confinement does not affect the lateral swelling of the ridges. Error bars represent standard deviation, n = 3.



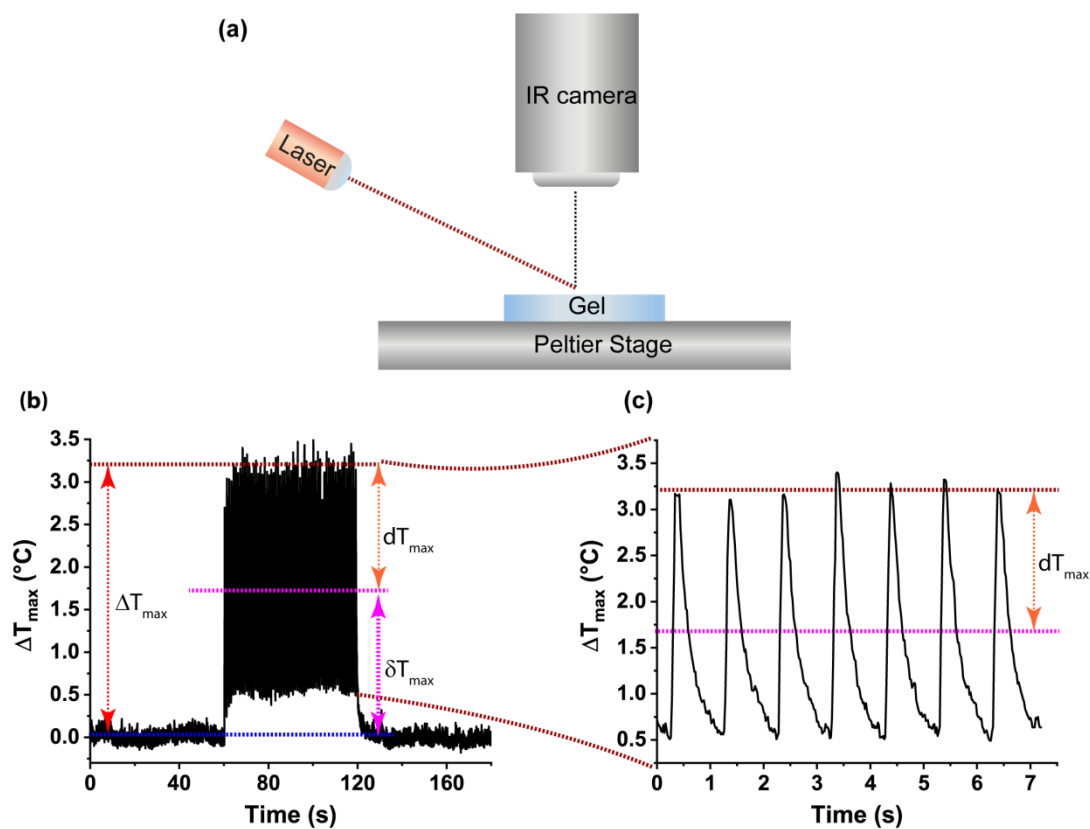
Supplementary Figure 4. Confocal images of swollen (at room temperature) 60/40 NIPAM/NEAM gels prepared with a topography of (a) 20 μm ridges separated by 100 μm valleys, with creases clearly visible in the valleys, and (b) 25 μm ridges separated by 25 μm valleys, where creases are not observed. Scale bar = 50 μm.



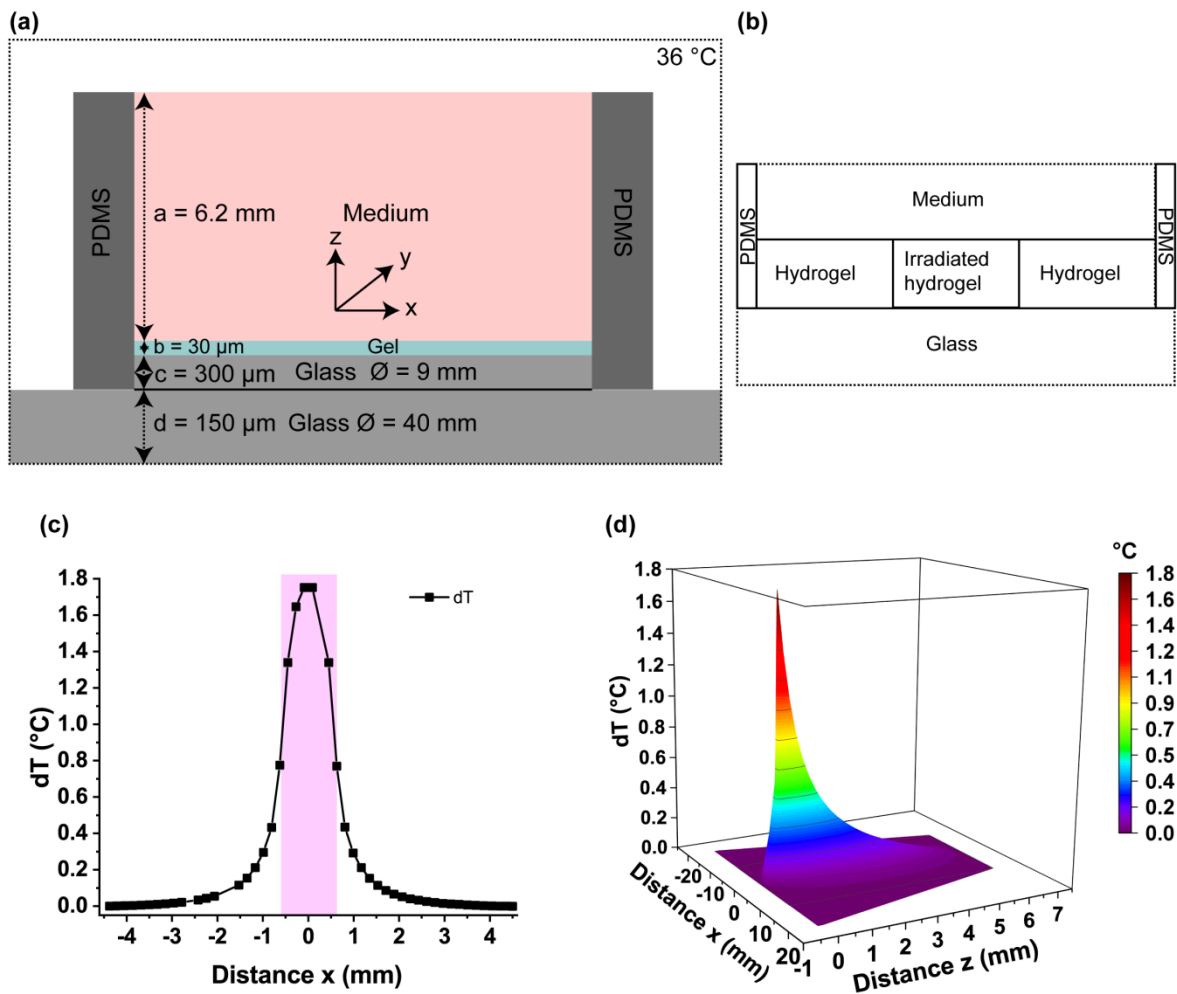
Supplementary Figure 5. (a) An illustration showing the average dimensions of the gold nanorods (AuNRs) used in the experiments, as derived from the (b) TEM images. (c-d) The UV-vis spectra of (c) the AuNRs dispersed in water and (d) the 60/40 NIPAM/NEAM gels without AuNRs and with AuNRs (gel precursor solution OD = 20) at different temperatures. (e) Quantification of the AuNRs using inductive coupled plasma-optical emission spectroscopy (ICP-OES) in the gel after preparation and after swelling, and in the swelling medium (water). No AuNRs are observed in the medium after 3 days, demonstrating that the AuNRs do not leach out from the gel. Error bars represent standard deviation, $n = 3$.



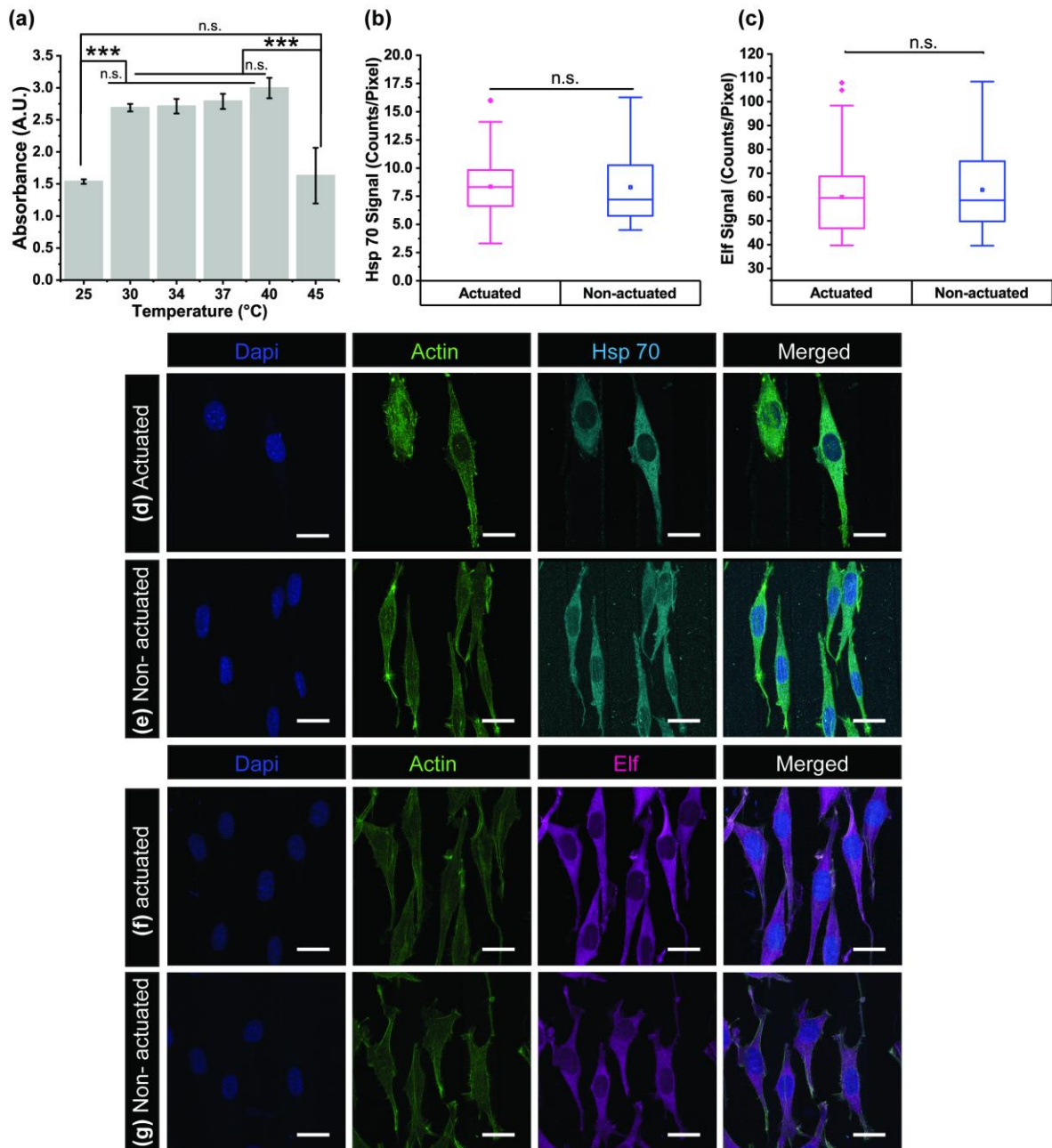
Supplementary Figure 6. Variation of the microstructure ridge width of 60/40 NIPAM/NEAM gels without AuNRs and with AuNRs (OD 100) in thermal equilibrium at different temperatures shows that the VPTT of the gels is not affected due to the addition of AuNRs. Error bars represent standard deviation, $n = 3$.



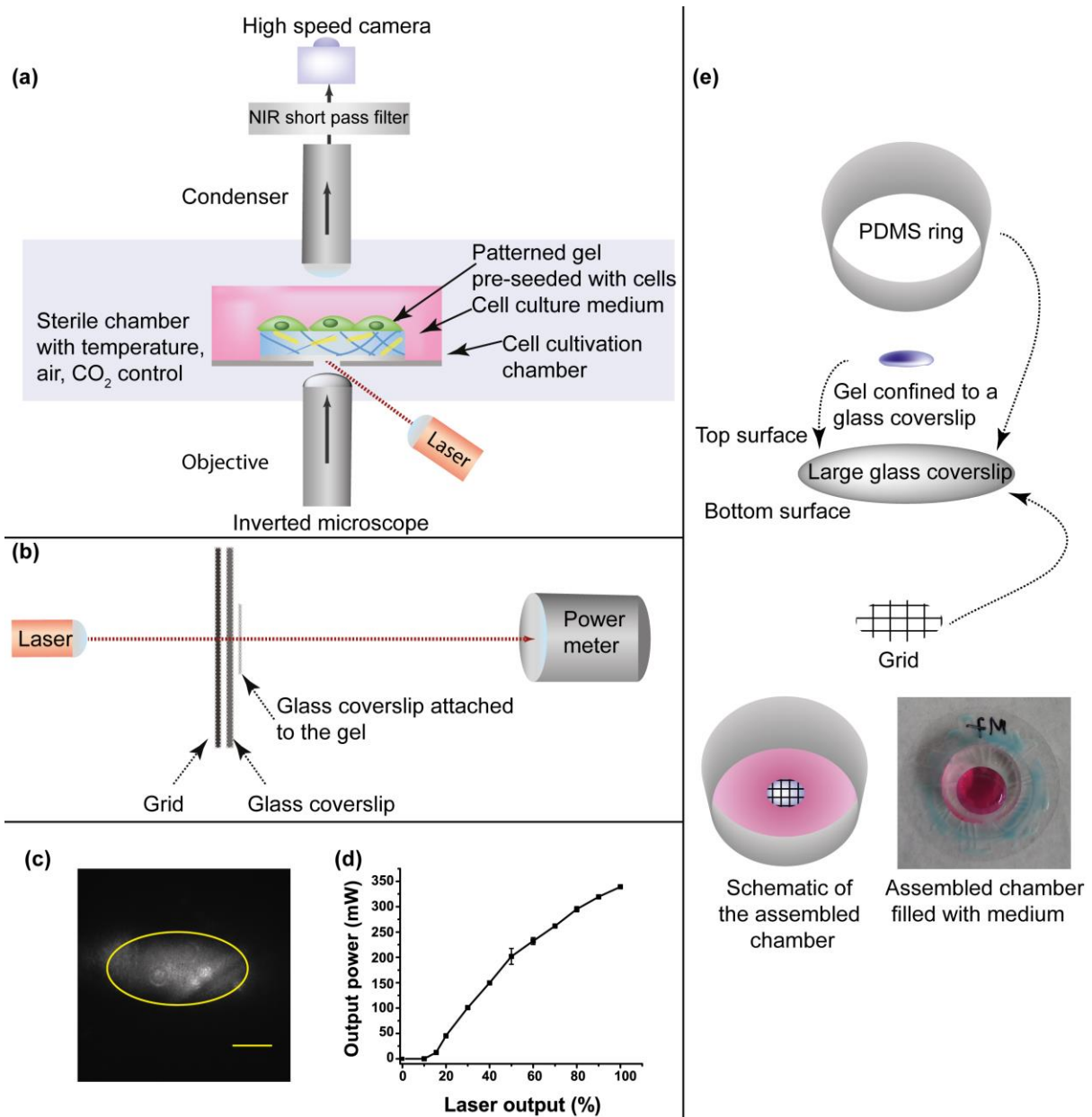
Supplementary Figure 7. (a) Schematic of the set-up used for measuring the gel temperature with an IR camera during photothermal heating. (b) The maximum temperature on the gel when the gel is stroboscopically irradiated from 60 - 120 s (340 mW, 1 Hz, 100 ms laser ON time). (c) The maximum temperature modulates with the pulse duration of the incident laser.



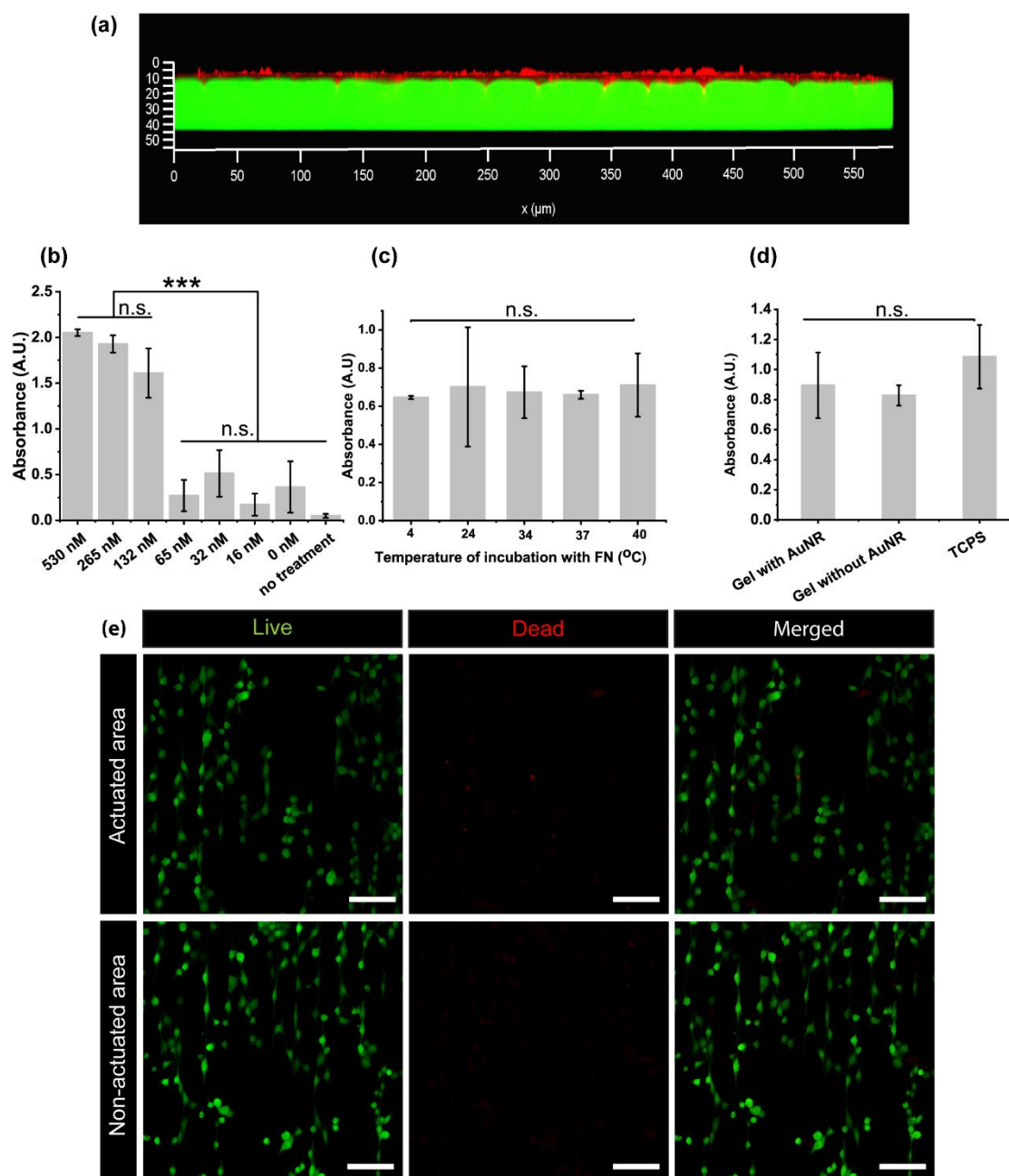
Supplementary Figure 8. (a) A schematic showing the dimensions of the setup that involves irradiation of the gel with NIR light. (b) A simplified version of (a) used for the purpose of the Finite Element Simulation. (c) Results of the simulation obtained for a time independent photothermal equilibrium that is achieved in response to a laser pulse of 340 mW, 100 ms laser ON time and 1 Hz frequency, depicting the variation of temperature at the surface of the gel. The laser spot is shown with the overlaid pink rectangle (d) A 3D distribution of the heat dissipation from the irradiated region of the gel. The asymmetric nature of the distribution in the z -direction stems from the difference in thermal conductivities of glass and medium (i.e. water).



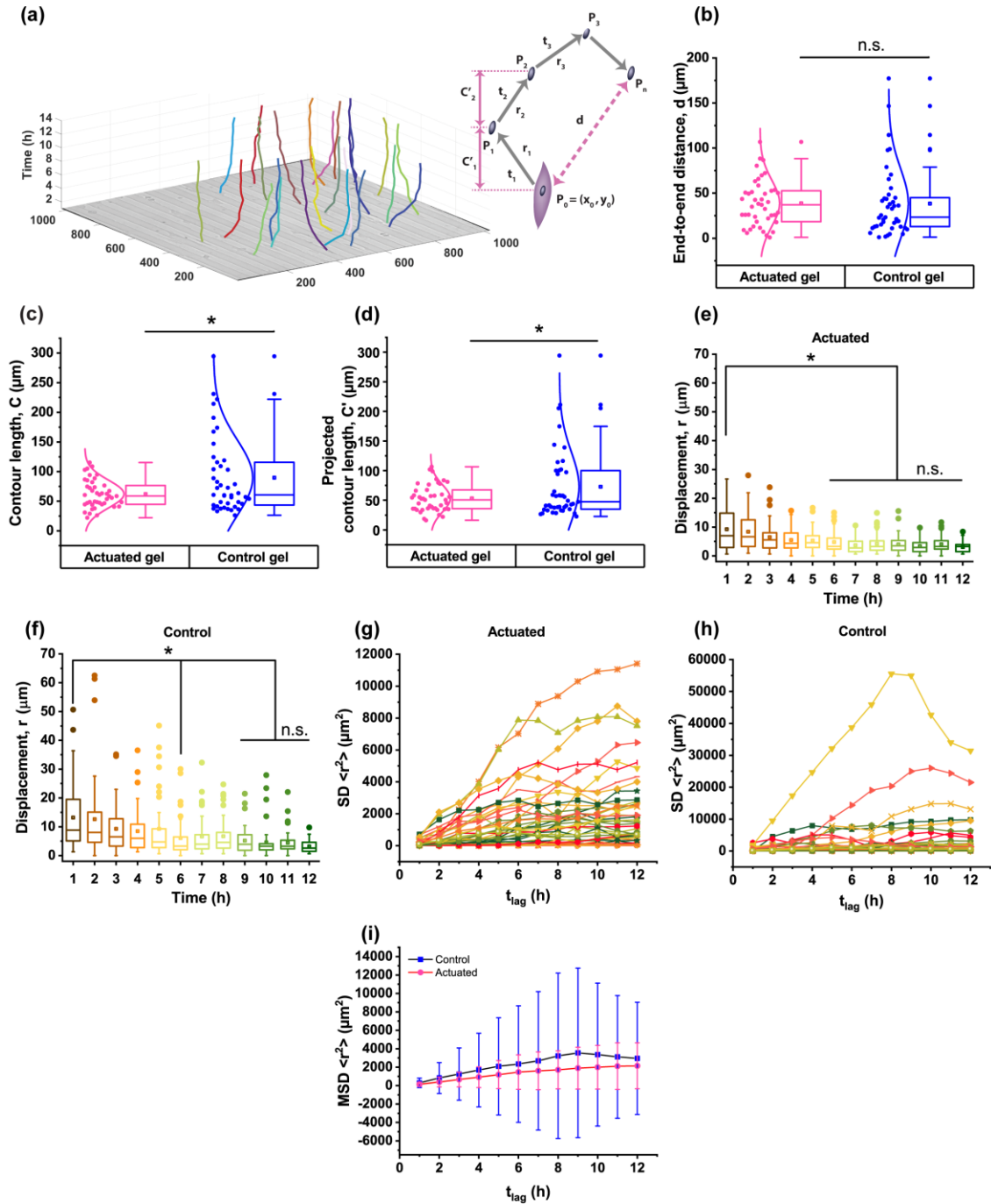
Supplementary Figure 9. (a) A representative MTS proliferation assay for L929 cells grown on TCPS after 24 h at different temperatures, $n = 3$. (b,c) The signal intensity of (b) heat shock protein Hsp 70 ($n = 2$, $N \geq 93$ cells) and (c) Elf (that stains against stress granules and P-bodies, $n = 2$, $N \geq 155$ cells) is shown in the box plots for actuated and non-actuated cells. (d,e) Representative images of cells stained against Hsp 70 (d) when actuated and (e) non-actuated, (f,g) against Elf that stains stress granules and P bodies for (f) actuated cells and (g) non-actuated cells. The non-actuation images are acquired from cells grown on the non-irradiated portion of the gel. In the box plots, the interquartile range (IQR) between the first and the third quartiles is indicated by the box, while whiskers denote 1.5 IQR. The hollow square, the horizontal line, and the filled dots represent the average, the median, and the outliers, respectively. Error bars represent standard deviation. *, **, *** are determined using one way ANOVA or Welch test, depending on the homogeneity of variances, and represent statistical significance at $p < 0.05$, 0.01 and 0.001, respectively. Scale bar = 20 μm .



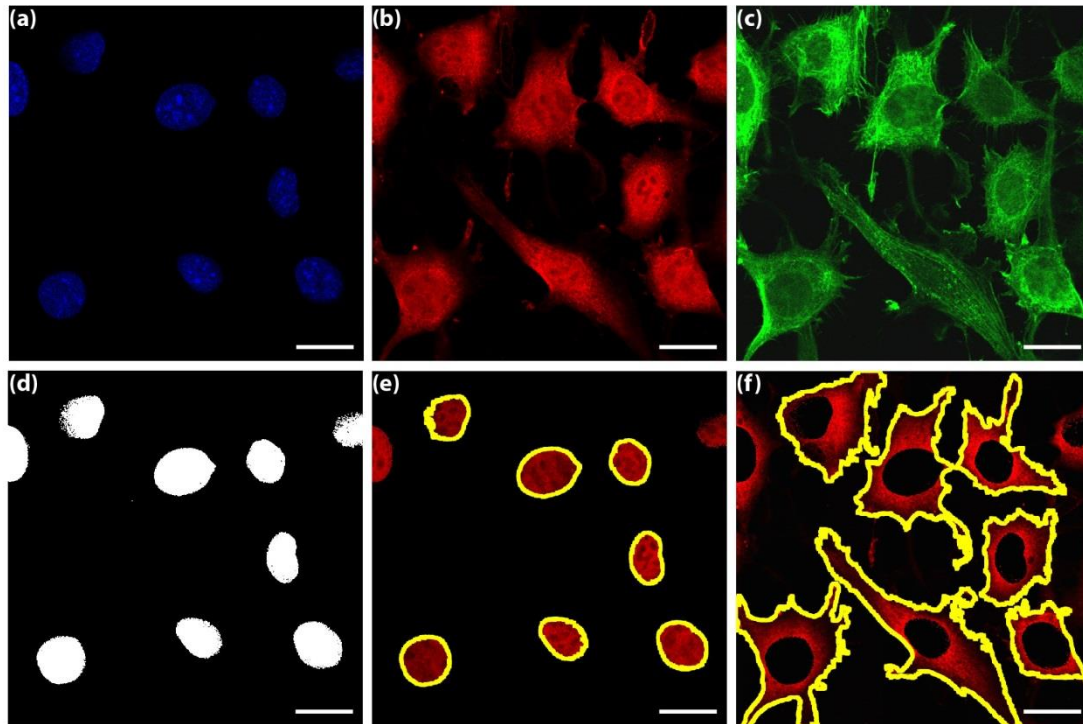
Supplementary Figure 10. (a) Schematic showing the microscope set-up, which is custom made for NIR actuation. A NIR laser is incident on the sample from the bottom. (b) Schematic of the set-up used to measure the laser power. (c) The laser footprint (340 mW) on the gel, scale bar = 500 μm . (d) The laser output profile, as measured with the power meter. (e) Schematic of the sample chamber designed for actuation. The gel, attached to a small cover glass, is glued on the sides to another larger glass coverslip and a PDMS ring is put around it to contain the media. On the opposite side of the glass coverslip, a grid with markings is glued to keep track of the actuated area. (*illustrations not to scale). Error bars represent standard deviation, $n = 3$.



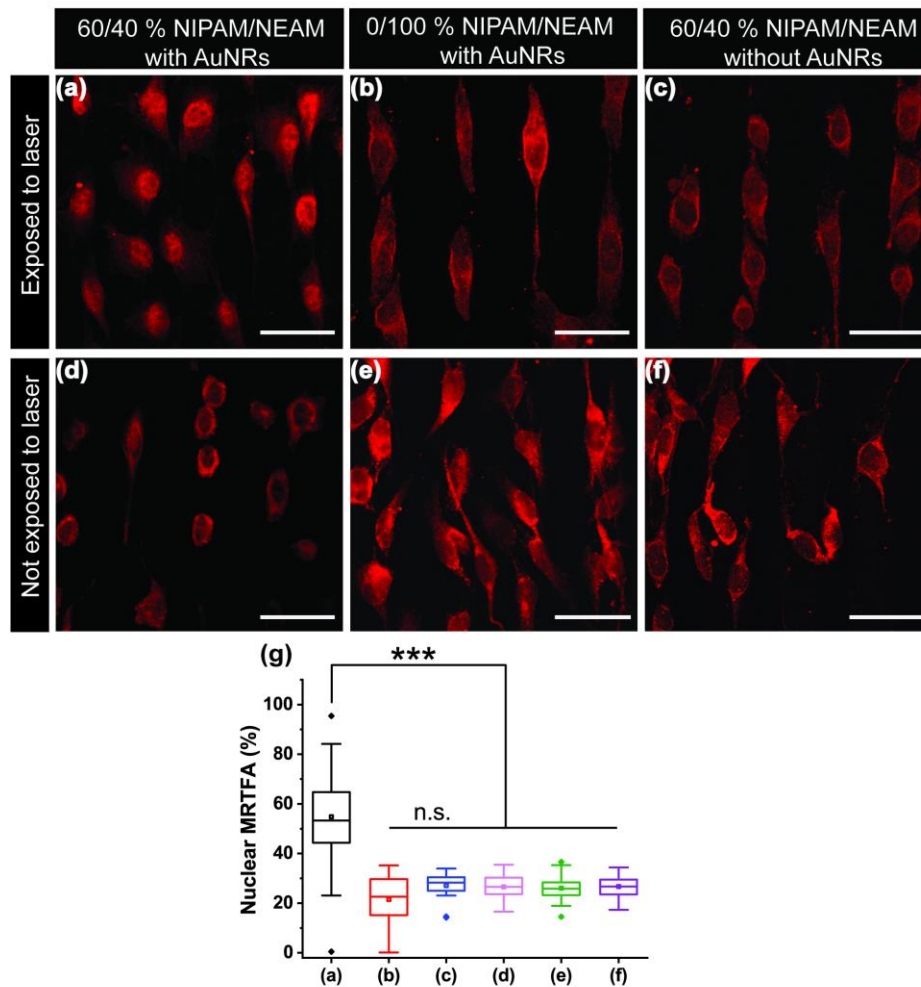
Supplementary Figure 11. (a) A confocal z-stack of a gel with fibronectin coating. Sulfo-SANPAH is used as a bi-functional crosslinker to covalently link fibronectin to the gel. Fibronectin is stained red, while the polymer is stained green. (b-c) The effect of the (b) fibronectin concentration and (c) temperature of fibronectin incubation on L929 cell proliferation. Based on these results, a fibronectin concentration of 265 nM, incubated at 34 $^{\circ}\text{C}$, is further used for this study. (d) When gels with an AuNR concentration of 0.004 vol % are prepared, the MTS assay does not show a toxic effect as AuNRs do not leach out of the gels. (e) Cells seeded on the gels are exposed to a pulsed laser (340 mW, 1 Hz, 100 ms laser ON time) for a period of 22 h. No significant cell death is observed in both the actuated and non-actuated regions of the gel. Scale bar = 100 μm . Error bars represent standard deviation, $n = 3$.



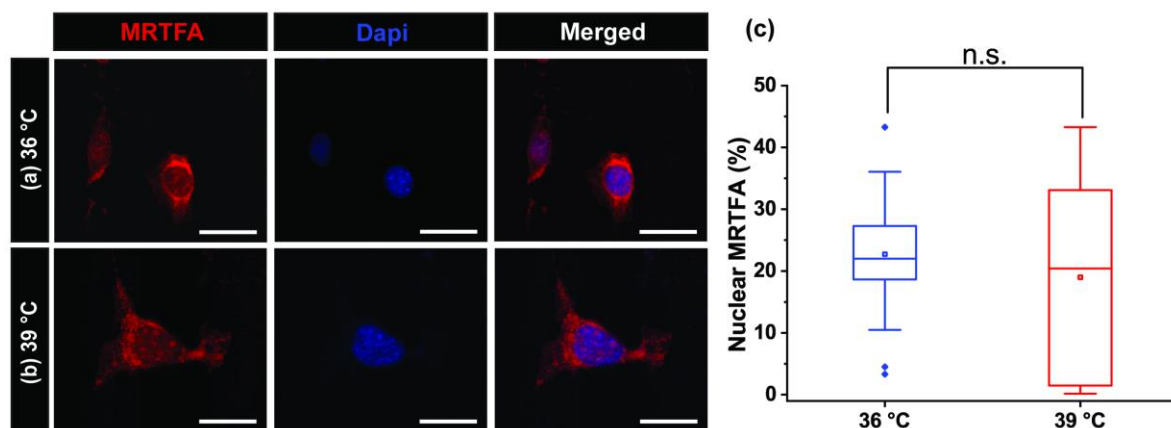
Supplementary Figure 12. (a) The trajectories of the individual cells that are traced over 12 h and a schematic showing the parameters to quantify cell motility. (b-d) Box plots showing cell motility parameters on 60/40 NIPAM/NEAM gels as a result of gel actuation (340 mW, 1Hz, 100 ms laser ON time, 12h), in comparison to non-actuating 0/100 NIPAM/NEAM control gels (b) the net displacement of L929 cells (end-to-end distance), (c) the total distance travelled by the cell (contour length) (d) the distance covered by the cell in the direction of the patterns (projected contour length). (e-f) The displacement (r) of the cells in intervals of 1 h, starting from $t = 0$ h for (e) actuated cells and (f) control cells, showing that cells slow down and cover less distances as time progresses. (g,h) The square displacements (SD) for all cells plotted for each lag times (g) for actuated cells and (h) for control cells. These values are averaged to get the mean of the SD (MSD) at each lag time, which is used to determine that cells undergo erratic motion (Figure 3 c). (i) The MSD of all the cells is plotted along with the standard deviation. The box plots show the result for each cell ($n = 2$, $N \geq 43$ cells). In the box plots, the interquartile range (IQR) between the first and the third quartiles is indicated by the box, while whiskers denote 1.5 IQR. The hollow square, the horizontal line, and the filled dots represent the average, the median, and the outliers, respectively. On the left of the box plot, all data points are shown, the normal distribution curve serves to guide the eye. *, **, *** are determined using one way ANOVA or Welch test, depending on the homogeneity of variances, and represent statistical significance at $p < 0.05$, 0.01 and 0.001, respectively.



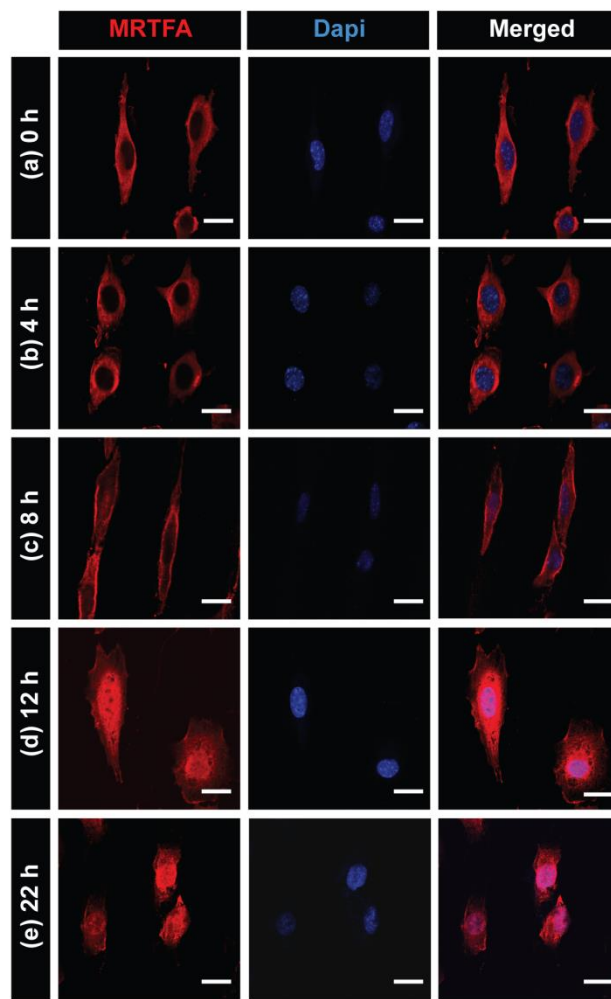
Supplementary Figure 13. Image processing for quantification of nuclear MRTFA (%) (a,b,c) The nucleus, MRTFA, and actin stained images, respectively. (d) Thresholded image of (a) that is used as a mask to determine nuclear and cytoplasmic MRTFA. (e,f) The nuclear and cytoplasmic distribution of MRTFA obtained after operating the boolean operators AND and Subtract on (b) and (d), respectively. Scale bar = 20 μm .



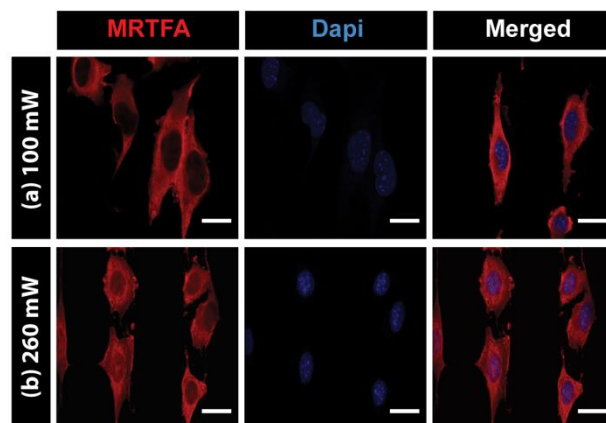
Supplementary Figure 14. Immunofluorescent staining for MRTFA in cells grown on (a,d) 60/40 NIPAM/NEAM gels with AuNRs which show photothermal heating with mechanical deformation (actuation), (b,e) 0/100 NIPAM/NEAM gels with AuNRs, which show photothermal heating without mechanical deformation, (c,f) and 60/40 NIPAM/NEAM gels without AuNRs, which do not display photothermal heating or mechanical deformation. The top row shows the region of the gels that is pulsed with NIR light for 12 h (340 mW power, 1 Hz, 100 ms laser ON time), while the bottom row shows a region of the gel that is not exposed to NIR light. The actuated region demonstrates translocation of MRTFA from the cytoplasm to the nucleus, while this is neither observed on the control gels nor in the regions of the gel that do not actuate. Scale bar = 50 μ m. (g) The nuclear MRTFA (%) is measured and represented by box plots where the interquartile range (IQR) between the first and the third quartiles is indicated by the box, while whiskers denote 1.5 IQR. The hollow square, the horizontal line, and the filled dots represent the average, the median, and the outliers, respectively. On the left of the box plot, all data points are shown, the normal distribution curve serves to guide the eye. ($n \geq 2$, $N \geq 18$ cells). *, **, *** are determined using one way ANOVA or Welch test, depending on the homogeneity of variances, and represent statistical significance at $p < 0.05$, 0.01 and 0.001, respectively.



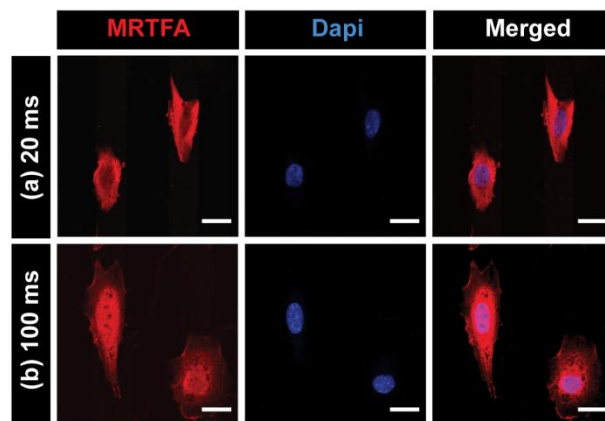
Supplementary Figure 15. Immunofluorescent staining for MRTFA in cells grown on 60/40 NIPAM/NEAM gels with AuNRs at (a) 36 °C and (b) 39 °C, where MRTFA is located in the cytoplasm at both temperatures. Scale bar = 20 μm . (c) Nuclear MRTFA (%) is measured and represented by box plots where the interquartile range (IQR) between the first and the third quartiles is indicated by the box, while whiskers denote 1.5 IQR. The hollow square, the horizontal line, and the filled dots represent the average, the median, and the outliers, respectively ($n = 3$, $N \geq 16$ cells). *, **, *** are determined using one way ANOVA or Welch test, depending on the homogeneity of variances, and represent statistical significance at $p < 0.05$, 0.01 and 0.001, respectively.



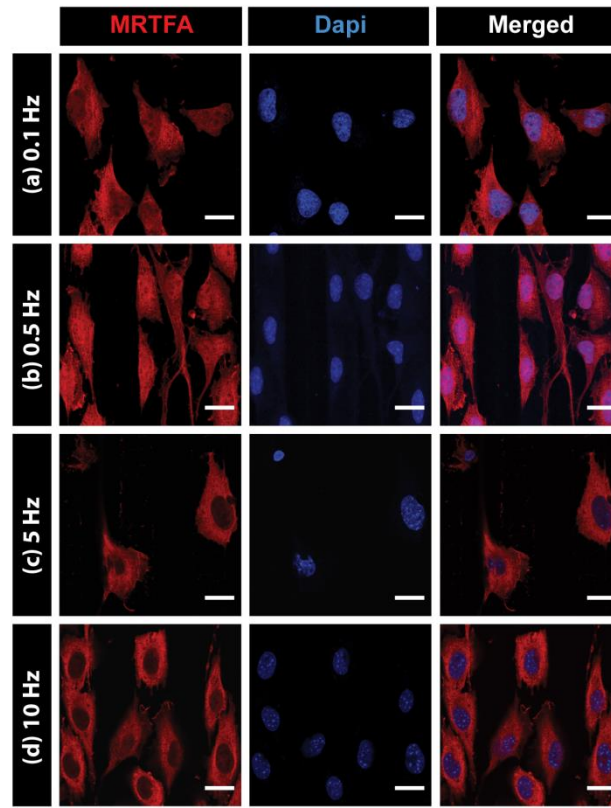
Supplementary Figure 16. Representative immunofluorescent images of cells that are present in the actuating area of the gel stained against MRTFA and Dapi (340 mW power, 1 Hz, 100 ms laser ON time) for (a) 0, (b) 4, (c) 8, (d) 12, and (e) 22 h. Scale bar = 20 μ m.



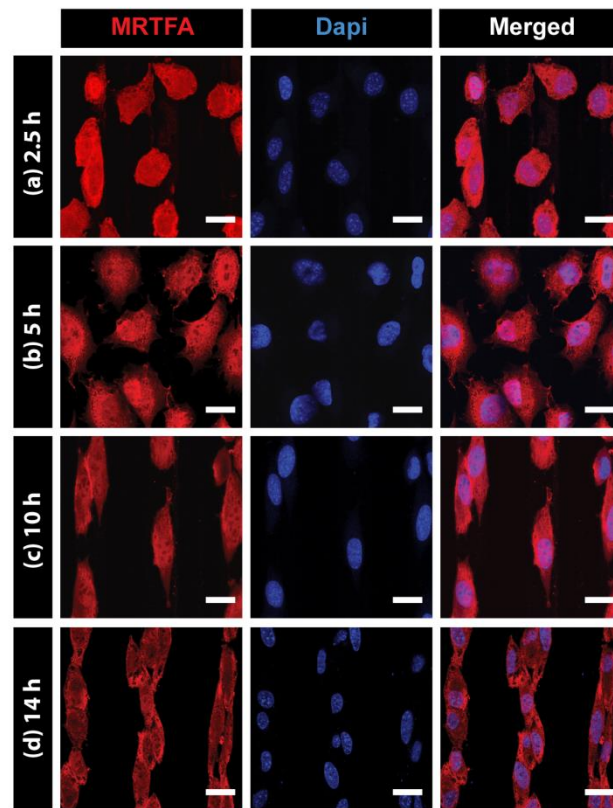
Supplementary Figure 17. Representative immunofluorescent images of cells that are present in the actuating area of the gel stained against MRTFA and Dapi (12 h, 1 Hz, 100 ms laser ON time) when the laser power is varied from **(a)** 100 mW to **(b)** 260 mW. Scale bar = 20 μ m.



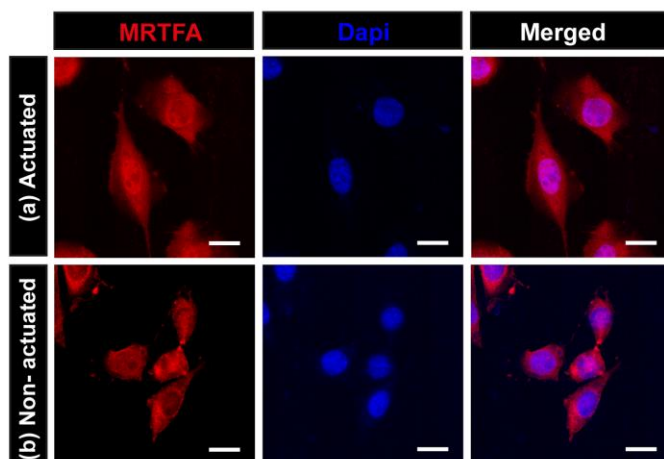
Supplementary Figure 18. Representative immunofluorescent images of cells that are present in the actuating area of the gel stained against MRTFA and Dapi (340 mW power, 1 Hz, 12 h) when the laser ON time of the pulse is varied from **(a)** 20 to **(b)** 100 ms. Scale bar = 20 μ m.



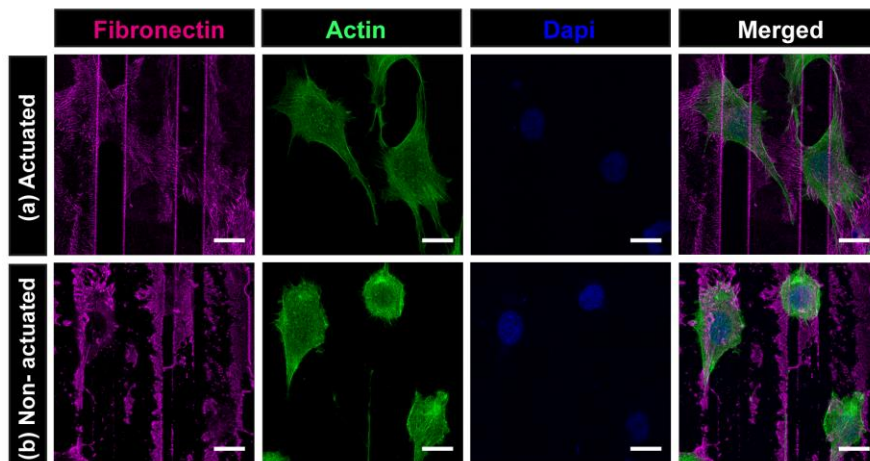
Supplementary Figure 19. Representative immunofluorescent images of cells that are present in the actuating area of the gel stained against MRTFA and Dapi (340 mW laser power, 12 h) with a pulse of 100 ms when the frequency is changed from **(a)** 0.1 to **(b)** 0.5 Hz, or with a pulse of 20 ms to achieve higher frequencies of **(c)** 5 and **(d)** 10 Hz. Scale bar = 20 μ m.



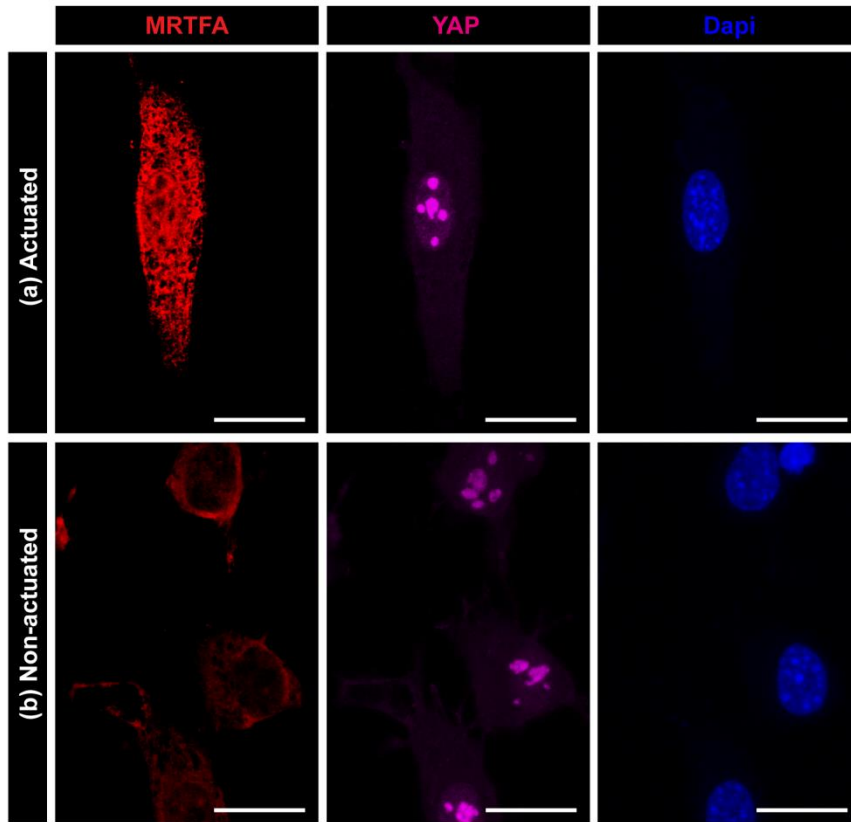
Supplementary Figure 20. Representative immunofluorescent images of cells that are present in the actuating area of the gel stained against MRTFA and Dapi (340 mW power, 1 Hz, 100 ms laser ON time, 12 h), after which the gel is relaxed for different time lengths before fixing and staining. The relaxation time is varied from (a) 2.5, (b) 5, (c) 10, or (d) 14 h. Scale bar = 20 μm .



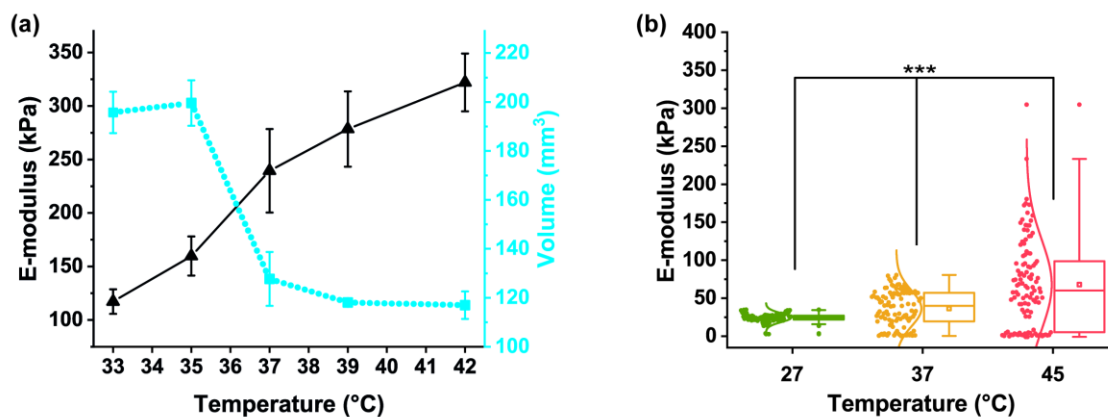
Supplementary Figure 21. Representative immunofluorescent images of cells that are present in the (a) actuating area (340 mW power, 1 Hz, 100 ms laser ON time) and (b) non-actuating area of a 60/40 % NIPAM/NEAM gel with AuNRs, functionalized with collagen I. MRTFA shuttles from the cytoplasm to the nucleus in response to 12 h actuation.



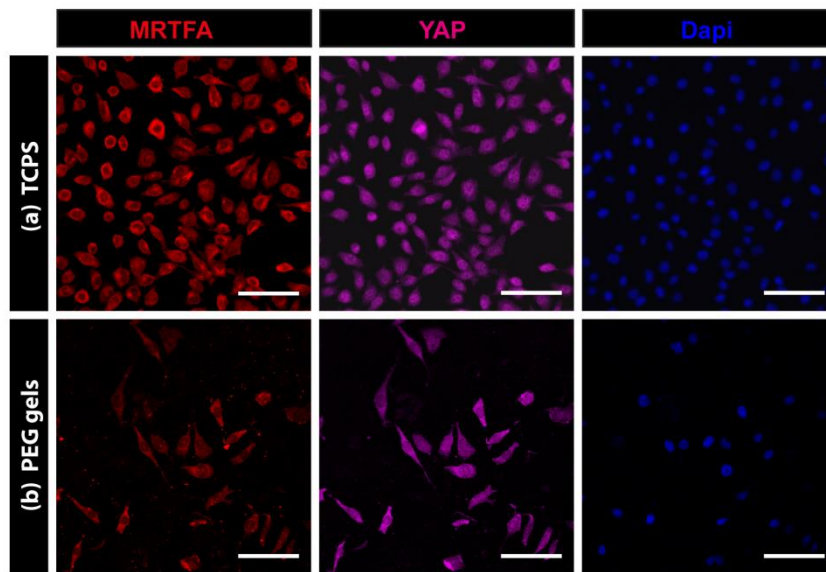
Supplementary Figure 22. Fibronectin secretion by cells grown on collagen coated gels that are **(a)** actuated for 12 h (340 mW, 1 Hz, 100 ms laser ON time) and **(b)** that are not actuated. The actuated cells also show aligned deposition of fibronectin, while a more random deposition pattern is observed for the non-actuated cells. Scale bar = 20 μ m.



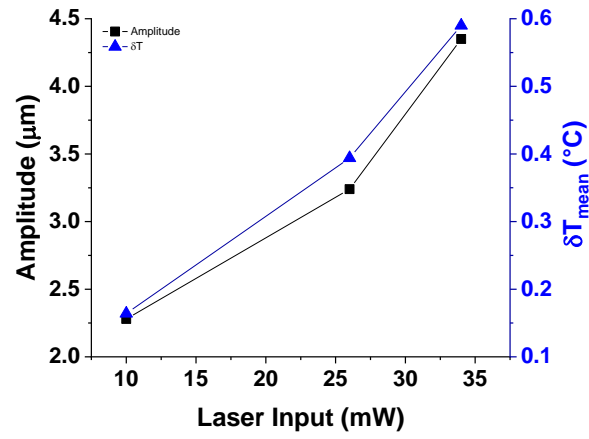
Supplementary Figure 23. Immunofluorescent images of cells that are present in the **(a)** actuating area (340 mW power, 1 Hz, 100 ms laser ON time) and **(b)** non-actuating area of a 60/40 % NIPAM/NEAM gel with AuNRs. While YAP is found in the nucleus in both cases, MRTFA shuttles from the cytoplasm to the nucleus in response to actuation. Scale bar = 20 μ m.



Supplementary Figure 24. (a) The compressive modulus of the bulk hydrogels is measured by monotonic compression at different temperatures and plotted with the volume of the hydrogels at the corresponding temperature, $n = 3$. (b) The local modulus of the confined gels tethered to a glass coverslip is measured using Atomic Force Microscopy (AFM), $n = 2$. The interquartile range (IQR) between the first and the third quartiles is indicated by the box, while whiskers denote 1.5 IQR. The hollow square, the horizontal line, and the filled dots represent the average, the median, and the outliers, respectively. On the left of the box plot, all data points are shown, the normal distribution curve serves to guide the eye. Error bars represent standard deviation. *, **, *** are determined using one way ANOVA or Welch test, depending on the homogeneity of variances, and represent statistical significance at $p < 0.05$, 0.01 and 0.001, respectively.



Supplementary Figure 25. MRTFA, YAP, and Dapi stained L929 fibroblast cells. **(a)** On tissue culture polystyrene, MRTFA is present in the cytoplasm, while YAP is localized in the nucleus. **(b)** On soft 1 wt % poly (ethylene glycol) gels, MRTFA and YAP are localized in the cytoplasm. Scale bar = 100 μ m.



Supplementary Figure 26. A plot of the temperature changes that are experimentally measured during photothermal actuation using an IR camera and the corresponding changes in amplitude when the laser input is varied.

Supplementary Tables

Polymers/Crosslinked Gels (mole %)	Solvent	LCST/VPTT (°C)
Linear Polymers		
100 % NIPAM ($M_n = 123,600$; PDI = 1.7)	Water	~33.9
90.2/ 9.8 % NIPAM/NEAM ($M_n = 154,600$; PDI = 2.0)	Water	~ 38.1
60/40 NIPAM/NEAM ($M_n = 95500$, PDI = 2.7)	Water	~ 59.4
Tethered gels		
100 % NIPAM	Water	~ 28
100 % NIPAM	RPMI Cell culture medium	~ 26
60/40 % NIPAM/NEAM	RPMI Cell culture medium	~ 36
Freestanding discs		
92/8 % NIPAM/NEAM	RPMI Cell culture medium	~ 28
80/20 % NIPAM/NEAM	RPMI Cell culture medium	~32.6
60/40 % NIPAM/NEAM	RPMI Cell culture medium	~ 38.3

Supplementary Table 1. A summary of the LCST/ VPTT values for different compositions of NIPAM/NEAM investigated in the present study as linear polymers, tethered gel films, or freestanding gel discs in water and cell culture media.

Laser power (mW)	T ON (ms)	T OFF (ms)	Duty cycle	frequency	Energy input (mJ)	Actuation amplitude (μm)	Relative displacement (%)	Estimated Force (nN)	Energy of actuation (pJ)
340	100	900	10	1	34	4.35	7.07	141.91	0.61
260	100	900	10	1	26	3.24	5.26	78.73	0.25
100	100	900	10	1	10	2.28	3.70	38.99	0.08
340	100	900	10	1	34	4.35	7.07	141.91	0.61
340	20	980	2	1	6.8	1.62	2.63	19.68	0.031
340	100	1900	5	0.5	17	4.35	7.07	141.91	0.617
340	100	9900	1	0.1	3.4	4.35	7.07	141.91	0.617
340	20	180	10	5	34	1.62	2.63	19.68	0.031
340	20	80	20	10	68	1.62	2.63	19.68	0.031

Supplementary Table 2. A summary of the different stroboscopic conditions for laser pulsing used in the present study, the amplitude of actuation, the calculated relative displacement, the generated forces as a result of actuation, and the energy of actuation per actuation cycle i.e. per beat. Also see Supplementary Method 8.

Parameter	Value	Units
Incident power	340	mW
Absorbance of the gel	0.068	N.A.
Gel thickness	30	μm
Spot area	1246400	μm^2
Spot radius	630	μm
Duty cycle	1:10	N.A.
k_{hydrogel}^1	0.624	$\text{Wm}^{-1}\text{K}^{-1}$
k_{glass}^2	1.127	$\text{Wm}^{-1}\text{K}^{-1}$
k_{PDMS}	0.15	$\text{Wm}^{-1}\text{K}^{-1}$

Supplementary Table 3. Laser and material parameters used for the simulation of the gel temperature

Supplementary Methods

Supplementary Method 1. Acryl silanization of glass coverslips

Glass coverslips (diameter = 9 mm, Merienfeld) are cleaned by sonication in water, acetone, and isopropanol for 5 min each, after which they are dried with nitrogen gas. The coverslips are activated with oxygen plasma for 15 min, 200 W, and an oxygen flow rate of 50 ml/min in a plasma coater (AK 330). After plasma treatment, the coverslips are silanized by keeping them in a desiccator at a pressure of 8×10^{-2} mbar with 100 μl of 3-(Trimethoxysilyl) propyl acrylate silane (Sigma) for 2 h. After 2 h, the silane is removed and the desiccator is maintained at a pressure of 8×10^{-2} mbar for 2 h. These acrylsilanized glass coverslips are placed in the dark in an oxygen free environment until further use.

Supplementary Method 2. Dispersion and quantification of AuNRs

Since AuNRs show a surface plasmon resonance, this property is used to quantify the amount of AuNRs in the solution. The optical density of the gel precursor solution, as well as of the hydrogels, is measured on a JASCO UV-Vis spectrophotometer from 1100 to 400 nm at 1000 nm/min. Quartz cuvettes with a path length of 1 mm are used to measure the absorbance. A gel precursor solution, which does not have AuNRs, is used as a reference solution. Hydrogels without AuNRs are used as reference for measuring the spectra of the gels. The number density of the AuNRs in the solution is calculated according to the following equation:

$$n = \frac{A \ln 10}{\sigma l},$$

Supplementary Equation 1

with

n = number density of the AuNRs per unit volume,

σ = extinction cross-section of the AuNRs, which is considered to be $6100 \text{ nm}^{2,3,4}$,

l = optical path,

A = absorption (A.U.)

The gels used in the present study are prepared from a precursor solution with an O.D. ~ 95 when calculated for a path length of 10 mm, which corresponds to $3.6 \text{ AuNRs}/\mu\text{m}^3$. To measure the spectra, gels are prepared on acryl silanized glass slides and dipped in a cuvette filled with cell culture medium. The dispersion of AuNRs in the gels is visualized by transmission electron micrography (Libra 120, Zeiss). For this purpose, very thin gels loaded with AuNRs (gel precursor solution OD 1.0) are prepared on carbon coated copper grids (PLANO, CF300-CU) and imaged.

Inductive Coupled Plasma-Optical Emission Spectroscopy (ICP-OES, ICP-atom emission spectrometer Plasma 400, Perkin Elmer) is used to determine the concentration of Au in the hydrogels with a reliable quantification limit of 50 mg/L. Hydrogels are dried at $40 \text{ }^\circ\text{C}$ for 48 h, ionized via consecutive nitric acid (65 %) treatment and hydrochloric acid (30 %) treatment in a microwave, and sequentially used for analysis.

Supplementary Method 3. Laser parameters and sample holder for actuation

Temperature variations in the gel are dependent on the incident laser power and the AuNRs in the gel. The laser power reaching the gel is estimated using Lambert-Beer Law.

$$\frac{P_{abs}}{P_0} = 1 - 10^{-A}$$

Supplementary Equation 2

Where P_{abs} , P_0 and A are the power absorbed by the gel, the incident power, and the absorbance (optical density, A.U.) of the gel, respectively. A gel with thickness $\sim 30 \mu\text{m}$ prepared from a precursor solution with O.D. 20 displayed an absorbance of 0.0527 at 37°C (Supplementary Figure 5). For a laser spot size of 1.2 mm^2 and a gel thickness of $30 \mu\text{m}$, this leads to a laser fluence (Laser power/gel volume) of $200\text{-}1030 \text{ W/cm}^3$,

The sample holder for actuation comprises a grid (Cell Lattice 63571), which is fixed with glue (Twin sil[®], Picodent) on one side of a coverslip ($\varphi = 40 \text{ mm}$), while the small glass coverslip ($\varphi = 9 \text{ mm}$), to which the gel is bound, is fixed on its sides with glue on the other side of the coverslip, such that the optical path is not obstructed by the glue. A PDMS ring is fixed around the gel to accommodate cell culture medium. The grid is used to identify the precise location of the actuated portion of the sample (Supplementary Figure 10). The laser power reaching the gel for different laser outputs is measured using a power meter with a similar optical path as used for the actuation experiments (Supplementary Figure 10 b,d).

Supplementary Method 4. Functionalization of the gel surface

The gel surface is covalently functionalized with fibronectin to promote cell adhesion using Sulfo-SANPAH mediated succinimide crosslinking. This protocol is adapted from^{5,6}. A stock solution of 0.1 M Sulfo-SANPAH in DMSO is prepared and stored at -80°C . The stock is diluted to a working solution of 3.38 mM in water just before use. After sterilization of the gels with ethanol and subsequent washing with water, $20 \mu\text{l}$ of Sulfo-SANPAH is added to the surface of each gel. To ensure uniform spreading of this solution on the gel surface, a glass coverslip is placed on top. All steps involving Sulfo-SANPAH are rapidly performed in the dark ($\leq 2 \text{ min}$) to avoid deactivation of Sulfo-SANPAH. The gel is then exposed to UV light (Konrad Benda, 8W) for 14 min . After exposure to UV light, the activated gels are thoroughly washed in excess water at least three times, and then incubated overnight with $15 \mu\text{l}$ fibronectin

at different concentrations and at different temperatures. After optimization, 265 nM fibronectin is incubated at 34 °C (Supplementary Figure 11). An incubation temperature of 34 °C is selected based on the cell morphology observed in the images (data not shown). The gels are again washed thrice with water and immersed in cell culture medium for ≥ 1 h prior to cell seeding. Immunofluorescent staining with anti-fibronectin primary antibody is used to confirm fibronectin binding to the surface of the gel. A concentration of 66 nM is used for collagen I coating.

Supplementary Method 5. Cell motility analysis

Each cell is assigned a position P_i at time t_i , where P_i is defined by Cartesian co-ordinates (x_i, y_i) . The distance between two positions P_i and P_{i+1} is denoted by r_i . Time lapse images obtained at an interval of 1 h are evaluated to measure the parameters listed below.

End-to-end distance (d_n): The net distance that is covered by the cell, thus the net displacement between the final and initial position P_n of the cell.

$$d_n = \Delta(P_0, P_n) \quad \text{Supplementary Equation 3}$$

Contour length (C_n): The actual distance covered by cells. This is usually greater than the net (end-to-end) distance, as cells do not follow a straight path. The contour length at time t_n is calculated as the sum of the distances between two consecutive positions, covered by the cells along their path till time t_n .

$$C_n = \sum_{i=0}^{n-1} r_i \quad \text{Supplementary Equation 4}$$

Cell migration rate (v): The migration rate for one cell is calculated as the distance covered by the cell within a time interval divided by the time interval.

$$v = \frac{C_n}{t_n - t_0} \quad \text{Supplementary Equation 5}$$

Persistence (L): The distance that the cell covers without changing its direction. To calculate this, the net displacement of the cell from the initial to the final position is divided by the sum of the total distance travelled to reach the final position. Hence, the persistence is the end-to-end distance divided by the contour length.

$$L = \frac{r_n}{C_n} \quad \text{Supplementary Equation 6}$$

Projected contour length (C'_i): The actuation is directionally controlled using a micro-patterned substrate. Therefore, the topography of the gel can also influence cell motility. To calculate the movement of cells in the direction of substrate micro-patterns, the projected contour length is calculated as the distance travelled by the cells in a direction parallel to the topography.

$$C'_i = \sum_{i=0}^{n-1} |y_{i+1} - y_i| \quad \text{Supplementary Equation 7}$$

To interpret the trajectory plots of cells (erratic or directed), the classical method of analysis using mean square displacement (MSD, $\langle r^2 \rangle$) as a function of lag time is used. (Supplementary Note 7).

Supplementary Method 6. Quantification of MRTFA, focal adhesions, stress granules and P bodies, heat shock protein 70, and fibronectin

Image analysis is performed using ImageJ software. Z-stack images of cells are converted into orthogonal maximum intensity projections. To quantify the nuclear MRTFA (%), Otsu's thresholding method is employed to create masks for nucleus and cell area from dapi and actin stained images, respectively. Z-stack images of cells are converted into orthogonal maximum intensity projections. To quantify the nuclear MRTFA (%), Otsu's thresholding method is employed to create masks for nucleus and cell area from dapi and actin stained images, respectively. The dapi mask and Boolean operators (SUBTRACT and AND operators for the area outside the nucleus and the nucleus, respectively) are used to create maps of MRTFA signal in the nuclear and cytoplasmic domains (Supplementary Figure13). Nuclear MRTFA

(%) is calculated from the raw intensity of MRTFA fluorescence signal in the nucleus and the cytoplasm. The fluorescence signal is assumed to be linearly proportional to the amount of MRTFA. Focal adhesions are quantified from the paxillin stained images using a trainable WEKA segmentation⁷ with particle analysis, and a threshold of $0.5 \mu\text{m}^2$ is set to remove noise. The Elf and the Hsp 70 signal is quantified per cell by determining the mean signal intensity after thresholding cells. Fibronectin signal intensity per cell is quantified by measuring the total signal intensity in a field of view (FOV) and by dividing it with the cell number obtained from dapi images, while the mean fibronectin intensity in a FOV is determined after thresholding from the mean signal intensity.

Supplementary Method 7. Determination of swelling properties

The swelling properties of the bulk hydrogels, used for mechanical testing, are evaluated to correlate the observed mechanical properties with the volume of the gel. After fabrication of the bulk hydrogels, they are immersed in excess DMSO to remove the unreacted monomers and washed in deionized water overnight. The gels are then immersed in cell culture medium at different temperatures and allowed to swell. The dimensions of the bulk hydrogels are measured using a Vernier Callipers at each temperature and the values are used to determine the mechanical properties.

Supplementary Method 8. Theoretical estimation of forces during actuation

To estimate the order of forces that are exerted on the cells, Hooke's law is employed, assuming that the actuation involves simple harmonic oscillations, where the driving force is provided by the incident energy from the laser. Newton's second law defines force as a quantity that can indirectly be assessed by measuring other mechanical properties, such as deformation and material properties⁸. The linear restoring elastic force (F) of a simple harmonic oscillator is given by $F = k * x$, where x is the displacement and k is the spring constant. Here, the spring

constant, $E * x$, is derived from the elastic modulus ($E = 30$ kPa) of the gel, as obtained from the AFM measurements at 37 °C, and hence, the equation may be modified to $F = E * x^2$, with x defined as half the amplitude. The energy of actuation i.e. the work done per actuation (W) is defined as $W = F * x$.

Supplementary Notes

Supplementary Note 1. Gel properties

While linear co-polymers of NIPAM/NEAM prepared by free radical polymerization in dioxane show an LCST of ~ 37 °C for 92/08 mole % NIPAM/NEAM, hydrogel films tethered to glass used in the present study have a VPTT of ~ 37 °C for a 60/40 NIPAM/NEAM molar ratio in cell culture media. Similar hydrogel films prepared with 100% NIPAM possess a VPTT of ~ 27 °C in media, compared to ~ 32 °C in water (Supplementary Figure 3b). The drop in VPTT can be explained by the presence of salts and proteins in the media.⁹ The VPTT of 37 °C observed for a hydrogel with 60/40 molar ratio of NIPAM/NEAM is non-intuitive as one would expect a higher VPTT based on this ratio. This may be explained by the higher sensitivity of NEAM to the presence of salts as compared to NIPAM, which is in agreement with previous observation where the VPTT of PNEAM decreased by ~ 20 °C in the presence of 1 M NaCl¹⁰. This drop in VPTT is higher compared to PNIPAM, for which variable values have been reported, ranging from a decrease of ~ 5 °C (PNIPAM)¹¹ to ~ 8 - 9 °C for gels¹² in the presence of 1 M NaCl. To check if the confinement of the hydrogel film influences the VPTT, free-standing discs are fabricated from a mould of diameter 30 μ m and height 5 μ m, using different molar ratios of NIPAM/NEAM (Supplementary Figure 3 c-e, Supplementary Table 1). By measuring their diameter at varying temperatures in media, a VPTT of ~ 38 °C is observed for free-standing (unconfined) 60/40 % NIPAM/NEAM hydrogel discs, which is slightly higher than the hydrogels tethered to a glass slide. This may be the result of confinement, as previously reported in literature¹³

In the collapsed state, the ridges (surface topography) of the hydrogel are rectangular (~ 25 μm width) and resemble the silicon wafer pattern, while in the swollen state, the ridges appear concave with ~ 32 μm width and the grooves acquire a reduced width of ~ 18 μm (Figure 1 d). The thickness of the dry gel is $3.2 \pm 0.7 \mu\text{m}$ (measured at the ridge). When performing volume phase transitions by successive heating and cooling cycles, there is no shift in the VPTT and thus no hysteresis is observed (data not shown), in contrast to pNIPAM in solution¹⁴. Monotonic compression of free-standing hydrogel discs at different temperatures demonstrates a rise in elastic modulus from 120 kPa at 33 °C to 320 kPa at 42 °C (dynamic mechanical analyser (DMA), Supplementary Figure 24), corresponding to hydrogel shrinking above the VPTT. In the physiologically relevant temperature range of 36-39 °C, the bulk elastic modulus varies between approximately 200 and 275 kPa. For confined hydrogel films tethered to the glass coverslips, atomic force microscopy (AFM) nano-indentation estimates the elastic modulus of the gels to range from ~20 to ~30 to ~ 60 kPa for varying temperatures from 27 °C to 37 °C to 45 °C, revealing that the elastic modulus only changes by a factor of ~1.5-2 (DMA and AFM, respectively) in the temperature range of interest (36 - 40 °C).

Supplementary Note 2. Gel surface topography

When preparing and confining flat gel films of a similar composition and thickness to a rigid substrate, creases are observed. However, in the case of the microstructured gels used here, the surface density and location of creases depend on the filling fraction of ridges relative to the microstructure period.

$$\text{Ridge filling fraction} = \frac{\text{Ridge width}}{\text{Ridge width} + \text{Valley width}} \quad \text{Supplementary Equation 8}$$

For filling fractions smaller than 0.5, creases are present in the valleys at a distance from the edge (Supplementary Figure 4). For example, creases are observed on gels prepared with 20 μm wide ridges that are separated by 100 μm valleys with a filling fraction of 0.16. For gels

with a filling fraction of 0.5, no creases are observed, even with high-resolution confocal imaging. Based on this observation, combined with the fact that creases are depleted from the edges of the ridges, it seems that the presence of ridges suppresses crease formation. Hence, the 25 μm ridges (similar in dimension to a cell), separated by 25 μm valleys, are selected for all experiments in this report.

In addition, a larger fractional change is measured in ridge width compared to the ridge height ($\Delta h/\Delta w \sim 0.3$). This is in contrast to a confined flat film, for which $\Delta h/\Delta w \geq 1$ is expected. Together with the absence of creases when the ridge filling fraction is sufficiently high, this may indicate weak confinement of the ridges relative to the bulk of the gel below the topography.

Furthermore, the swelling ratio of the ridges is compared with the swelling ratio of free-standing discs, prepared from the same 60/40 NIPAM/NEAM composition and a diameter of 30 μm . This reveals a lateral swelling ratio of ~ 1.8 in case of the ridges, which is only marginally larger than the change in diameter of the free swelling discs (~ 1.6) (Supplementary Figure 3). This shows that although the ridges are connected to the surface of a tethered hydrogel film, their swelling and shrinking ability in response to temperature changes is not compromised.

Supplementary Note 3. Photothermal actuation

Considering the length scales involved in this photothermal hydrogel system, the AuNRs are ~ 140 times smaller in dimension than a typical cell (assumed to have a size of $\sim 10 \mu\text{m}$). Moreover, the generated heat can be controlled using a pulsed laser, which enables tunable gel actuation, depending on the kinetics of the gel's phase transition. In response to the incident laser, the AuNRs heat up the surrounding medium and gel within nanoseconds to reach a steady state⁴. The characteristic time for swelling/shrinking (τ_{charac}) in the irradiated portion of the

gel can be estimated based on the theory of kinetic swelling of gels and the collective diffusion coefficient, D_{gel} ¹⁵.

$$\tau_{charac} = \frac{\alpha^2}{D_{gel}} \quad \text{Supplementary Equation 9}$$

with α = linear size of the smallest dimension. Assuming that D_{gel} for PNIPAM gels is $\sim 4.0 \times 10^{-7} \text{ cm}^2\text{s}^{-1}$,¹⁶ the characteristic time for swelling/shrinking of a 60/40 NIPAM/NEAM hydrogel film with 30 μm height is estimated to be $\sim 23 \text{ s}$ at 36 °C. On the other hand, the thermal equilibration time of the gel required to reach a steady temperature due to the photothermal effect depends on the thermal diffusivity of water ($k = 1.4 \times 10^{-3} \text{ cm}^2\text{s}^{-1}$) (τ_{rel} , *rel* stands for relaxation).

$$\tau_{rel} = \frac{\alpha^2}{k} \quad \text{Supplementary Equation 10}$$

Using Supplementary Equation 10, the typical time for the irradiated gel spot to reach an equilibration temperature is estimated to be $\sim 6.4 \text{ ms}$. As the stroboscopic irradiation is performed with duty cycles (ON time) ranging from 20-100 ms, the thermal equilibration process is assumed to be complete. Hence, thermal confinement is avoided due to heat diffusion out of the target area into the surrounding cell culture medium and the gel swells and shrinks⁴. Thermal confinement is undesirable as it can lead to very high temperatures in the exposed area of the gel and impair actuation¹⁷. Due to the large heat sink, the temperature in the medium or in the non-exposed portion of the gel does not increase, leading to local actuation only in the target area. The laser pulses are selected to avoid overheating of the sample and keep the mean temperature in the actuated area always below 38.5 °C. However, since the laser ON (20 or 100 ms) and OFF time (80-900 ms) are shorter than the characteristic time required for shrinking and swelling of the gel (τ_{charac} , 23 s), respectively, the gel is modulated around a steady state during actuation but does never fully shrinks or swells (Movie 5).

Supplementary Note 4. Estimation of gel temperature

To enable visualization of the initial contraction when the laser is turned on and the final swelling when the pulsing is stopped, the laser is pulsed between 60 and 120 s (100 ms pulses, 340 mW). Figure 2 shows that there is a spatial distribution of temperature changes, confined to the laser spot. The local total increase in temperature, ΔT_{mean} , can be subdivided in to two parts: the overall increase in the steady state temperature compared to the initial state when the laser is OFF (δT_{mean}) and the additional fluctuations in temperature when the laser is ON (dT_{mean})

$$\Delta T_{mean} = \delta T_{mean} \pm dT_{mean} \quad \text{Supplementary Equation 11}$$

From the mean temperature measurements, the estimated values are $\delta T_{mean} \sim 0.6$ °C and $dT_{mean} \sim 0.3$ °C leading to a net ΔT_{mean} of ~ 0.9 °C. Besides the average temperature, we also measure the maximum temperature during actuation (Supplementary Figure 7). This is the maximum temperature recorded in the gel and does not reflect the temperature of the entire gel.

$$\Delta T_{max} = \delta T_{max} \pm dT_{max} \quad \text{Supplementary Equation 12}$$

The maximum total temperature increase ΔT_{max} in the irradiated portion of the gel is approximately 3.0 °C at equilibrium, with $\delta T_{max} \sim 1.7$ °C. The maximum temperature (due to positive oscillations) around the new equilibrium (dT_{max}) is around ~ 1.5 °C, keeping the maximum temperature experienced by the cells below 39.0 °C and thus below the temperature of heat shock for cells¹⁸. Therefore, no portion of the gel is over-heated beyond the hyperthermia temperature, even after prolonged actuation. While the temperature increases very quickly leading to a rapid collapse, the recovery is slower during one actuation cycle (Movie 5).

In addition to the temperature measurements using an IR camera, the changing ridge width of the gel during actuation is measured, demonstrating a ridge width of ~ 32 μm before light

exposure and a change in ridge width from ~ 31.7 to 27.4 μm and vice-versa during actuation. Based on the calibration curve correlating the ridge width with temperature, obtained when the gels are heated without light in medium and at thermal equilibrium (Figure 1 e), the temperatures are calculated to be ~ 35.7 $^{\circ}\text{C}$ before actuation and alter between ~ 36 and 39 $^{\circ}\text{C}$ during the laser pulse (340 mW power, 1 Hz, 100 ms ON time). This measurement method is in close agreement (within experimental error) with the IR-measured temperatures, and hence, an adverse effect of temperature on cells is prevented.

Supplementary Note 5. Simulation of heat dissipation from the hydrogel film in response to a NIR laser

Local actuation of the gel is driven by local temperature changes. The temperature changes are kept at a minimum to prevent overheating of the gel, which can lead to adverse effects on cells. Infrared imaging is used to measure the temperature changes that occur in the irradiated zone on the gel. However, it is well known that time dependent measurements of the local temperature resolved in three dimensions in such small volumes are prone to error. To gain more insight into the heat dissipation during photothermal heating of this system, heat transfer is modeled using finite element modeling.

In this basic model, all time dependent variations of the system, such as volume changes and the increase in the AuNR density that occur due to the collapse of the gel are ignored. Based on the results from the infrared experiments, it is assumed that a steady state is rapidly reached during irradiation ($t <$ laser ON time). Therefore, heat diffusion and the temperature distribution across the gel surface is calculated for the situation after photothermal equilibrium is achieved. It is assumed that heat conduction dominates the scene (thus convection and radiation are neglected) and that the media and the side border of the gel are in thermal equilibrium with the environmental chamber (temperature constant at 36 $^{\circ}\text{C}$). Another assumption is that the power

absorbed by the AuNRs is uniformly distributed over the volume of the irradiated gel, resulting in an isotropic heat flux from the irradiated volume at any time.

The actuation chamber consists of the gel that is covalently attached to a small glass coverslip (diameter = 9 mm, thickness = 300 μm), which is in turn fixed on a larger glass coverslip (diameter = 40 mm, thickness = 150 μm) with an assumed perfect contact. The hydrogel is a film (height 30 μm at 36 $^{\circ}\text{C}$) on top of the 9 mm glass coverslip and is assumed to be dominated by water. A central 1.2 mm^2 spot is irradiated with the laser and the average heat flux is calculated based on the incoming power and the geometry of the spot. To estimate the temperature distribution, an imaginary surface is added above the gel across the heat chamber, 500 nm above the gel where cells are expected to grow, and is divided into 50 points. The topography present on the surface of the gel is neglected and the diffusion of photothermal heating from an infinite hydrogel film that is placed on a glass coverslip and immersed in water is simulated. The Fourier equation is converted into the formalism of finite element method¹⁹ giving the following equation to solve:

$$\int_v -k\nabla T \nabla v dV = \oint_A q v dA \quad \text{Supplementary Equation 13}$$

where v is the variation function in the mesh, vanishing at the boundary, $v(A) = 0$, T is the temperature, V is the volume, q is the heat flux incident on the sample, which is 0 everywhere outside the area of irradiation, A is the area exposed to the laser i.e. the heat source. The outer boundary of the sample is at 309.15 K (36 $^{\circ}\text{C}$).

The material parameters used in the simulation are listed in Table 3. The gel is irradiated using laser pulses of 100 ms at 1 Hz, with a laser power of 340 mW. The absorbance value of a gel prepared from a precursor solution with OD 100 is used to calculate the power reaching the surface of the gel, P_{abs} as determined by the Lambert-Beer law (Supplementary Method 3) Using the parameters mentioned above, the heat intensity for a duty cycle of 10 % is given by

$$Q = \frac{P_{\text{abs}}}{\text{Central area}} \approx 1875 \text{ W/m}^2$$

Supplementary Equation 14

The simulations show that the average temperature of the irradiated area is ~ 1.8 °C higher than the surrounding temperature. This is in very close agreement with the IR temperature measurements revealing a $\Delta T_{\text{mean}} \sim 1$ °C. The heat dissipation over the hydrogel in the z direction (Supplementary Figure 8 d) is asymmetric, suggesting that a major part of the heat is dissipated through glass. This finding is also significant for cells, as it conveys that cells are not exposed to elevated temperatures.

Supplementary Note 6. Surface functionalization of the gel to support cell growth

Physisorption of fibronectin to the gel does not result in a uniform coating and leads to inhomogeneous cell growth (data not shown). Therefore, Sulfo-SANPAH is used as a bi-functional crosslinker to covalently bind the primary amines of fibronectin using succinimide chemistry (Supplementary Method 4)²⁰. The presence of fibronectin on the surface is confirmed via an anti-fibronectin antibody (Supplementary Figure 11) and the optimal concentration of fibronectin for the growth of L929 mouse fibroblast cells is 265 nM, as a further increase does not significantly increase cell attachment and growth after 2 days. In addition, neither the temperature (4 - 40 °C), at which fibronectin is incubated, nor the presence of AuNRs, affect adherence and proliferation of fibroblasts. The latter is not surprising as the AuNRs do not leach out into the medium.

Supplementary Note 7. Analysis of cell migration trajectories

A decrease in migration rate upon actuation is reflected in the contour length (sum of the distance covered by the cells in each step). Furthermore, the migration rate estimated by the

displacement in every hour decreases significantly over time for both cases (Supplementary Figure 12 e,f).

The effect of persistence is reflected in the contour length (distance covered by the cells) and the end-to-end distance of the trajectories (the net displacement of the cell from time $t = 0$ h to $t = 12$ h, Supplementary Figure 12 a-d).

The trajectories of single cells are analyzed by calculating the mean-squared displacement (MSD) as a function of lag time²¹. The MSD reflects the average end-to-end distance that is traversed by the cells during the lag time interval. In this study, the displacement (r) is calculated from time lapse frames acquired at time intervals (Δt) of 1 hour (13 frames acquired over 12 h, including the initial time $t = 0$). The squared displacement (SD) for a defined lag time equals the square of the end-to-end distance between $t = 0$ and $t = n\Delta t$, with n ranging between 0 and 12. The MSD $\langle r^2 \rangle$ at a given lag time $n\Delta t$ is calculated as the mean of the squared displacements (SD) for all cells ($N = 43$ cells) using Supplementary Equation 15

$$\text{MSD } \langle r^2 \rangle = \frac{1}{N} \sum_{i=1}^N [P_{i,(n\Delta t)} - P_{i(0)}]^2 \quad \text{Supplementary Equation 15}$$

Where $P_t(x,y)$ is the position vector of the cell at time t , described by the Cartesian coordinates (x,y) . Comparing the motion to particle diffusion²², the mean squared displacement shows the characteristics of anomalous subdiffusion. However, due to the high standard deviation of the data, no fitting is possible. The trajectories also indicate persistence related to the microstructure of the surfaces and an increase of this persistence in correlation to the mechanical actuation of the gels.

Supplementary References

- 1 Touloukian, Y. S., Liley, P. & Saxena, S. Thermophysical properties of matter-the tprc data series. volume 3. thermal conductivity-nonmetallic liquids and gases. (Thermophysical and electronic properties information analysis center (1970).
- 2 Powell, R., Ho, C. Y. & Liley, P. E. *Thermal conductivity of selected materials*. Vol. 8 (US Department of Commerce, National Bureau of Standards Washington, DC (1966).
- 3 Jain, P. K., Lee, K. S., El-Sayed, I. H. & El-Sayed, M. A. Calculated absorption and scattering properties of gold nanoparticles of different size, shape, and composition: applications in biological imaging and biomedicine. *The journal of physical chemistry B* **110**, 7238-7248 (2006).
- 4 Qin, Z. & Bischof, J. C. Thermophysical and biological responses of gold nanoparticle laser heating. *Chemical Society Reviews* **41**, 1191-1217 (2012).
- 5 Wang, Y.-L. & Pelham Jr, R. J. in *Methods in enzymology* 298 489-496 (Elsevier, 1998).
- 6 Kandow, C. E., Georges, P. C., Janmey, P. A. & Beningo, K. A. Polyacrylamide hydrogels for cell mechanics: steps toward optimization and alternative uses. *Methods Cell Biol.* **83**, 29-46 (2007).
- 7 Arganda-Carreras, I. *et al.* Trainable Weka Segmentation: a machine learning tool for microscopy pixel classification. *Bioinformatics* **33**, 2424-2426 (2017).
- 8 Roca-Cusachs, P., Conte, V. & Trepast, X. Quantifying forces in cell biology. *Nat. Cell Biol.* **19**, 742 (2017).
- 9 Becerra, N. Y., López, B. L. & Restrepo, L. M. Thermosensitive behavior in cell culture media and cytocompatibility of a novel copolymer: poly (N-isopropylacrylamide-co-butylacrylate). *Journal of Materials Science: Materials in Medicine* **24**, 1043-1052 (2013).
- 10 Lowe, J. S., Chowdhry, B. Z., Parsonage, J. R. & Snowden, M. J. The preparation and physico-chemical properties of poly (N-ethylacrylamide) microgels. *Polymer* **39**, 1207-1212 (1998).
- 11 Zhang, Y., Furyk, S., Bergbreiter, D. E. & Cremer, P. S. Specific ion effects on the water solubility of macromolecules: PNIPAM and the Hofmeister series. *J. Am. Chem. Soc.* **127**, 14505-14510 (2005).
- 12 Park, T. G. & Hoffman, A. S. Sodium chloride-induced phase transition in nonionic poly(N-isopropylacrylamide) gel. *Macromolecules* **26**, 5045-5048 (1993).
- 13 Harmon, M. E., Jakob, T. A., Knoll, W. & Frank, C. W. A surface plasmon resonance study of volume phase transitions in N-isopropylacrylamide gel films. *Macromolecules* **35**, 5999-6004 (2002).
- 14 Halperin, A., Kröger, M. & Winnik, F. M. Poly (N-isopropylacrylamide) phase diagrams: fifty years of research. *Angewandte Chemie International Edition* **54**, 15342-15367 (2015).
- 15 Tanaka, T. & Fillmore, D. J. Kinetics of swelling of gels. *The Journal of Chemical Physics* **70**, 1214-1218 (1979).
- 16 Tanaka, T., Sato, E., Hirokawa, Y., Hirotsu, S. & Peetermans, J. Critical Kinetics of Volume Phase Transition of Gels. *Physical Review Letters* **55**, 2455-2458, doi:10.1103/PhysRevLett.55.2455 (1985).
- 17 Vogel, A. & Venugopalan, V. Mechanisms of Pulsed Laser Ablation of Biological Tissues. *Chem. Rev.* **103**, 577-644 (2003).
- 18 Song, A. S., Najjar, A. M. & Diller, K. R. Thermally Induced Apoptosis, Necrosis, and Heat Shock Protein Expression in Three-Dimensional Culture. *Journal of Biomechanical Engineering* **136**, 071006-1-071006-10 (2014).

- 19 Font, R. & Peria, F. The Finite Element Method with FreeFem++ for beginners. *Electronic Journal of Mathematics & Technology* **7** (2013).
- 20 Sunyer, R., Jin, A. J., Nossal, R. & Sackett, D. L. Fabrication of hydrogels with steep stiffness gradients for studying cell mechanical response. *PloS one* **7**, e46107 (2012).
- 21 Qian, H., Sheetz, M. P. & Elson, E. L. Single particle tracking. Analysis of diffusion and flow in two-dimensional systems. *Biophysical journal* **60**, 910-921 (1991).
- 22 Manzo, C. & Garcia-Parajo, M. F. A review of progress in single particle tracking: from methods to biophysical insights. *Reports on progress in physics* **78**, 124601 (2015).